SELF-INVERSE TRANSFORMING PSEUDO NON-MOVING PARTS INTERFEROMETER: A THEORETICAL AND EXPERIMENTAL ANALYSIS

By

KAILASH SWARNA

Bachelor of Science
University of Madras
Madras, India
1983

Master of Science
Oklahoma State University
Stillwater, Oklahoma
1988

Submitted to the Faculty of the
Graduate College of the
Oklahoma State University
in partial fulfillment
of the requirements for
the degree of
DOCTOR OF PHILOSOPHY
December 1991

SELF-INVERSE TRANSFORMING PSEUDO NON-MOVING PARTS INTERFEROMETER: A THEORETICAL AND EXPERIMENTAL ANALYSIS

Thesis Approved:

M G Rockley

Thesis Adviser

J. Paul Devlin

Thomas C. Collins

Dean of the Graduate College

ACKNOWLEDGEMENTS

I wish to express my sincere gratitude to my major adviser Dr. Mark G. Rockley, for his guidance and assistance in the completion of this study and the continued support throughout my graduate career. The time spent in his research laboratory has been fruitful and most stimulating. I appreciate his support of the unique nature of my graduate program.

I wish to thank the other members of my committee, Dr. Neil Purdie, Dr. J. Paul Devlin, and Dr. Bruce J. Ackerson, for their patience and support. The financial support from the Department of Chemistry during the course of my graduate studies is appreciated.

I would like to thank Dr. Don Thompson, Dr. Gilbert Mains, Dr John Gelder, and Dr. Corrina Czekaj for their encouragement and support. Among the numerous friends that made my life in Stillwater enjoyable, Jim (pep) Peploski, Scott McCullough, Alison Marks, Karen Bintz, Tommy Sewell, Eric Wallace, Ann Ratcliffe, Alan Engle, Carol Engle, Theresa Hall, and Mark Fisher are indeed special. I also wish to thank Bharath and Sriram, two friends whose friendship I shall always cherish.

The enduring love of Nirmala and Ravishankar was instrumental in the successful completion of this degree. Rajam and Savithri (patti) have always been

supportive. Their genuine concern for my well-being is greatly appreciated.

The constant support of the members of my family, in particular my grandparents, warrants special mention. My parents were extremely supportive and made many sacrifices to enable the pursuit of my higher education. My dear father Vasanth, whose untimely death in 1987 deprived me of a good friend, was always the source of my inspiration and was instrumental in my decision to pursue graduate studies. His belief in my abilities and the constant encouragement to pursue my aspirations will always be remembered. His absence leaves a void that is hard to fill. I dedicate this humble piece of my life to his memory.

Sumathi, my dearest wife and friend, deserves much of the credit for the successful completion of this work. The long hours and days she has spent assisting me in completing this work are but a fraction of her true contribution to this effort. I am extremely thankful for the patience, love, and support Sumathi has always shown, particularly in the last two years. Her unshakable confidence in my abilities to fulfill this task added strength to my spirits and resolve. Our accomplishments together have been most fulfilling and we eagerly look forward to more challenges in life and shorter telephone bills.

TABLE OF CONTENTS

Chapter Page

LIST OF TABLES

Table Page

LIST OF FIGURES

CHAPTER I

INTRODUCTION

The evolution of analytical techniques in the physical and biological sciences has reached new heights in recent times. Several sophisticated techniques now exist which make qualitative and quantitative analysis of chemicals in a wide range of systems, both biological and other, a rather routine matter. Chemical detection and analysis which would have been impossible just a few years ago, is now carried out with automated ease and precision. New methods are announced with periodic regularity, and combined with the increased power and sophistication of electronics and computer systems find their way into the research lab with astonishing speed.

Yet, there exist a few applications, all of them very important, which seem to baffle and render unusable many of these same new techniques. There are usually two major reasons as to why this is so - firstly, many of these applications involve operations under a host of inhospitable conditions - conditions under which all but the hardiest of common laboratory instrumentation would cease functioning and, secondly, the high initial cost and high cost of maintenance and operation of such instrumentation (1).

More prominent among this group of applications are the early detection of chemical warfare agents in the battlefield, detection and monitoring of environmental contaminants under a variety of conditions, process and quality control in an inhospitable industrial setting, and detection and monitoring of common industrial pollutants such as flue-gases at their source. Each of these situations has been addressed at length by the global scientific community and several innovative technological advances have resulted from these efforts (2).

A possible solution to these environmental detection problems that has gained wide acceptance recently is the development of low cost, low power-consumption instrumentation that is capable of operating in a wide range of hostile conditions and is capable of delivering certain minimum performance requirements. Such efforts have led to extraordinary advances in optical interferometry and its spectroscopic applications. Chemical analysis with high sensitivity and efficiency has become a reality due to the development of Fourier Transform (FT) methods in IR, NMR, microwave, and mass spectroscopy (4). In particular, the development and wide acceptance of the now ubiquitous FTIR spectrometer has led to intensified efforts in developmental work in FT spectroscopy for the UV-Vis and near IR spectral regions, (5) which have remained the domain of dispersive spectrometers.

Of the many different types of analytical techniques now in use for applications ranging from chemical identification and characterization to medical diagnostics, spectroscopic techniques such as the group of optical spectroscopies (UV-Vis, IR), mass spectroscopy, and NMR etc. are perhaps the most common

Among these, infrared spectroscopy has had the greatest impact in the widest range of applications, primarily due to the rich spectral detail commonly available in the infrared region of the spectrum. In the late sixties and early seventies, infrared spectroscopy was considered to be a dying instrumental technique. Its revival as a premiere analytical technique and its present prominence are in large measure due to the development of Fourier Transform Infrared Spectroscopy (FTIR) that resulted from the intensive research efforts in optical interferometry (1).

It is likely that there is much to be gained by applying Fourier methods for spectroscopic applications in this spectral range. This conclusion is based on the significant advantages that this technique offers over dispersive methods. In addition to the Jacquinot and Fellget advantages (discussed in the following sections), these advantages include reduction of spectral errors due to stray radiation, rapid scanning times, wavelength precision, and reduction in the size and cost of basic optical equipment (12). This is based on experimental evidence obtained through the extensive application of FT methods in IR spectroscopy.

Many of the applications outlined above could be categorized as routine applications, wherein critical research grade performance levels such as very high spectral resolution are often not required. The resolution of a spectrometer, be it in any spectral region, has been a cause for much concern among spectroscopists. Yet, U.S. military specifications consider a resolution of 2 cm^{-1} from about 800 cm^{-1} to 1200 cm^{-1} to be acceptable for most of their field applications (2). Of greater importance in such applications is a fact recognized very early in the development and history of interferometers - because of their small size and weight, interferometers are suitable for field studies. The further reduction in size and complexity of interferometers can only serve to enhance this very useful feature. This would enable emission studies of several types to be carried out more readily in the field. For example, the throughput advantage of the interferometers makes it possible to study very weak sources, such as interstellar bodies. Studies of atmospheric pollution from remote vehicles such as balloons and aircraft would also benefit (3).

The void created by the inapplicability of existing instrumentation to some of the new problems discussed earlier is growing rapidly and must be filled in a reliable manner. It is this genuine need for the rapid development of low cost, high efficiency analytical instrumentation that has provided the impetus for the present work. The design, development, and characterization of a novel optical interferometer for applications in the IR, and possibly, the UV-Vis spectral regions is described. This interferometer has one "pseudo" moving part and accomplishes spectral acquisition through optical, rather than computational methods. This interferometer has the potential for application in a very rugged spectrometer with a compact design, simple operation and maintenance procedures, and will be significantly less expensive and consume much less power than existing systems.

Classification of Interferometers

There are many types of optical interferometers, with applications ranging from astronomy to spectroscopy and holography (7). This has led to the classification of interferometers into different categories, sometimes based on the applications for which they are designed. In general, interferometers may be classified in two ways: by the number of interfering beams and by the method used for beam separation. In the former classification, the two main categories are two beam interferometers and multi-beam interferometers, while in the latter, the two main categories are wavefront splitting interferometers and amplitude splitting interferometers (6).

Wavefront splitting interferometers make use of the fact that one way of obtaining two beams from a single source is to use two separate portions of the original wavefront. The superposition of these wavefronts at a later time will produce interference. Interference by amplitude splitting is achieved by the division of the amplitude of the same section of the wavefront obtained from a single source, hence producing two beams (8). This study is primarily concerned with amplitude splitting interferometers.

Amplitude Division

A beam of light from a single source can be divided into two portions by allowing part of the wave to be reflected off a surface and part to be transmitted. The transmitted and the reflected waves would have amplitudes which would be some portion of the original wave - which is to say that the amplitude has been split. A recombination of these wavefronts at a detector would result in interference, so long as the original coherence has not been destroyed. The clarity of the interference fringes seen will depend on the relationship between the coherence length and the path difference (9). As long as the path difference is less than the coherence length, fringes of good clarity will be observed.

Coherence Characteristics

The coherence characteristics of the radiation under study in a particular interferometric system are of great importance. A beam of quasimonochromatic light resembles a series of randomly phased, finite wavetrains which are very nearly sinusoidal (8). There is some variation in the frequency and the amplitude but this is slow compared to the rate of oscillation (about 10^{15} Hz). The time for which a given wavetrain exists is the coherence time, given by the inverse of the frequency bandwidth.

Mathematically,

$$\Delta t_c = \frac{1}{\Delta \nu}$$

where Δt_c is the coherence time, $\Delta \nu$ is the frequency bandwidth, and c is the speed of light, then the coherence length is given by

$$\Delta x_c = c\Delta t_c$$

Thermal sources have very short coherence lengths, often only about a few mm while laser sources can have coherence lengths of the order of several meters, and in some cases even several km.

Spatial coherence is a measure of the effects due to the finite spatial extent of practical light sources. If the spatial extent of the source is such that two distinct points on it are separated by a distance greater than the wavelength of light, then the lightwaves emitted from the two points will not have any definite phase relationship. Such an "extended" source would generally be considered to be incoherent (9). Thus, the spatial coherence of a given source is expressed in terms of the coherence length, the finite physical distance from a given point on the source for which two wavetrains emitted from two different points on the source are perfectly in phase.

Fourier Transform Spectroscopy

Fourier Transform Spectroscopy (FTS) is a spectroscopic technique derived from interferometry. The importance of FTS as an analytical tool in the infrared spectral range arises from two fundamental advantages it offers over conventional (non-FTS) spectroscopic methods. These two advantages, Fellget's or the multiplex advantage and Jacquinot's or the throughput advantage, form the basis for the widespread application of FTS in infrared spectroscopy. Fellget's advantage addresses the multiplex nature of an interferometer. In an interferometer, information from the entire spectral range of a given source is received simultaneously and is available for the entire duration of a scan of the interferometer. By contrast, in a grating spectrometer, only a narrow band of spectral information is available at any given instant in time (1).

However, this advantage of an interferometer based spectrometer is significant only in comparison with the case of a detector-noise limited grating spectrometer. A comparison between spectrometry in the UV-Visible region where dispersive systems are still largely used, and in the mid-IR region, where interferometric systems are heavily employed, shows that a major difference between the two methods lies in their detection systems. Detectors employed in the UV-Vis region can have noise equivalent to a few photons received per second. Then the noise in such spectral regions is usually due to statistical fluctuations in the source intensity, the so called "shot noise". In this case there is no multiplexing advantage since noise in the detector is not the limiting noise source, so a dispersive spectrometer may be just as efficient as a FT spectrometer. However, the throughput or Jacquinot advantage of the FT spectrometer is still present, and this may warrant the use of this technique (10).

Jacquinot's advantage addresses the ability of an interferometer to gather larger amounts of the incident energy than grating interferometers. This advantage, expressed in terms of the étendue (light gathering power) of an interferometer, states that for a given collimated incident beam, an interferometer has a greater solid angle and thus greater étendue, than a grating spectrometer.

Étendue is a measure of the light-gathering power or the throughput, of the interferometer (11). It is expressed in terms of an invariant value for a given optical system, and in this form provides a valuable tool for making meaningful comparisons between the optical efficiency of different systems. A more detailed explanation of étendue is provided later.

Interferometers in FTS

The most common interferometer used for FTS is the Michelson interferometer or some modification of its original design. The Michelson interferometer is a two mirror, amplitude splitting interferometer, with one of the mirrors mounted such that it can be moved along an axis parallel to the optical axis, thus generating the path difference necessary to observe interference (Fig. 1.1). The quality of the design of the mechanical drive system used to produce the variation in path difference in the interferometer ultimately determines its performance as well as its cost (1).

The complexity and high cost of existing FTIR systems is due in part to the presence of a significant number of moving parts - specifically the moving mirror and the attendant mechanical drive system. Interferometers designed for low resolution far-IR spectroscopy have the lowest overall design tolerance requirements for the drive mechanism in the interferometer. The tolerances of the drive mechanism for medium resolution mid-IR spectroscopy are much more stringent. This contributes to the high cost of existing FTIR instrumentation and

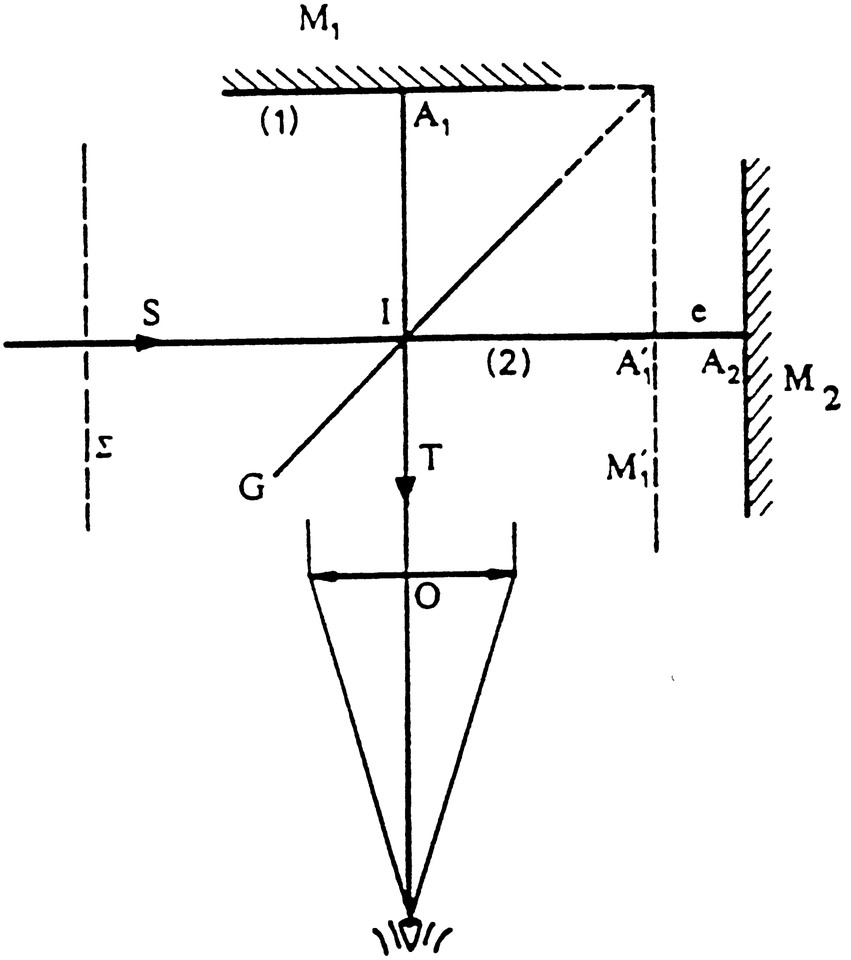

Figure 1.1 A schematic diagram of a Michelson interferometer. Here M_1 is the stationary mirror, M_2 is the moving mirror, S is the source, and O is the plane of observation.

the relative lack of instrumentation for the near-IR and UV-Vis spectral regions (14). Added to this is the expensive computing and electronic equipment needed to operate the instrument, and to compute the final spectrum. The quality of the interferometric drive system is the ultimate determinant of the performance of the interferometer and the ability to apply a given design to a particular spectral region.

There have been several studies measuring the detrimental effects of a poor drive mechanism on the overall performance of an interferometer. Specifically, Zachor (15) has presented a thorough review on the effects of a poor drive mechanism on the performance of an interferometer.

The detrimental effects of a poor drive mechanism in an interferometer are similar to the effects of beam divergence in the interferometer. Specifically, if the drive mechanism introduces errors in the alignment of the moving mirror with respect to the plane of the beamsplitter, the precise angle between them may change in an unstable manner. Consider the following example, which illustrates this phenomenon. If a mirror tilt of β radians is introduced in an interferometer irradiated with a collimated beam of radiation of diameter D, and wavelength λ, there is a concomitant change in the path difference for the extreme rays of the collimated beam. If this change in the path difference of one extreme ray over the other is represented by x, we have

$$x = 2D \, Tan \, \beta$$

and for small values of β,

$$x = 2D\beta$$

The contrast of the interference fringes, which depends on both the wavelength of the incident wavelength, and the path difference, begins to decrease when the change in the path difference x, is close to $0.1\,\lambda$. Thus, if the resolution of the interferometer during a scan with a misaligned mirror is not to be seriously degraded, the following condition must hold:

$$x < \frac{\lambda_{\min}}{10} = \frac{1}{10\sigma_{\max}}$$

$$= \quad \beta < \frac{1}{20D\sigma_{\max}}$$

where $\sigma_{\max}$ is the maximum wavenumber (frequency) in the spectrum. Thus, tolerances for the mirror drive become increasingly tighter as one goes from the far-infrared to the near-infrared and into the visible and UV regions of the spectrum. In conventional Fourier-Transform methods, the requirement of high accuracy scanning mechanisms severely restricts the design and the practical application of FT systems. These systems are also quite sensitive to mechanical shocks and require continuous alignment. The absence of such sensitive drive systems would make the optical system smaller in size and would greatly increase stability, and decrease the complexity of such instruments. The absence of moving parts or other forms of mechanical instability could also lead to the application of such interferometric systems to spectroscopic studies in the UV-Vis and near IR regions of the spectrum where high mechanical stability is required. Further, if the final spectra could be computed by optical rather than computational methods, additional simplification could be achieved. All these factors would provide a significant reduction in the cost of such systems. There has been a concerted effort by many research groups to address this technical challenge and some progress has been made in designing simplified instrumentation.

One innovative recent design for FT spectroscopy which has potential to meet the demands of field use in the UV-Vis and near-IR spectral regions is the non-moving-parts interferometer (16). Such an interferometer employs mirror tilt as a means of producing the desired path difference. One of the mirrors in the interferometer is tilted by a very small angle about an axis perpendicular to the optical axis. This tilt leads to the generation of a small path difference between the beams in the interferometer leading to the generation of interference. This path difference is a function of the tilt of the mirror and has a unique value for a given tilt angle. Thus, the mirror can be tilted to a given angle, left stationary, and the resulting static interference pattern at the output of the interferometer (a function of the tilt angle and the wavelength(s) of the source) recorded by a photodiode array detector. The signal received at the detector is a spatial intensity distribution and a record of this intensity distribution as a function of its position with respect to the detector element is recorded. This signal on transformation yields the desired spectrum.

The use of non-moving-parts interferometers in spectroscopy can be traced back to the work done by Leith, Upatnieks and Haines (17), who in 1965 used the wavefront reconstruction method as a means of magnification. The significance of their work as it applies to spectroscopy is that they were able to achieve modulation of a spatial carrier with the diffraction pattern from an object and due to a small difference in the angle of the two beams striking the screen, were able to record a Young's interference pattern. Stroke and Funkhouser (18) reported a method of Fourier Transform Spectroscopy using holographic imaging in 1965. In their method they used a modified Michelson-Twyman-Green interferometer to obtain the spectrum of Mercury. A significant point in this experiment was that the system used was a stationary interferometer, and further, no computation was necessary to obtain the spectrum. Saccocio (19), in 1967, used Lloyd's mirror in X-ray holography. He was able to record fringes on a photographic plate using the characteristic copper K radiation at 1.54 Å. This led to a possibility, at least theoretically, of being able to reconstruct spectra from these fringes. In 1968, Kamiya, Yoshihara and Okada (20), were able to successfully reconstruct atomic emission spectra of cadmium and mercury from holograms obtained with Lloyd's mirror. Yoshihara and Kitade (21) improved on the experiment performed by Stroke and Funkhouser and reported the use of a triangle path interferometer to obtain the holographic spectrum of a Mercury lamp. In 1971 Dohi and Suzuki (22) reported the attainment of high resolution holographic spectroscopy using a holographic interferometer without an imaging lens system. In the same report they also outline a method using heterodyning techniques for holographic spectroscopy. Yoshihara, Nakashima, and Higuchi (23) reported the use of a Mach-Zehnder interferometer to obtain the holographic spectra of Mercury and Cadmium in 1976. Okamoto, Kawata, and Minami (24) described yet another Fourier-Transform spectrometer with no mechanical moving parts. In their system, the interferogram was generated spatially using a triangle common path interferometer. The interferogram was detected by a self-scanning photodiode array.

In 1985, Barnes reported the application of a non-moving parts, square path Sagnac interferometer equipped with a self scanned photodiode array to obtain absorption and emission spectra in the visible region of the spectrum (25). Barnes, Eiju, and Matsuda (26) have used a similar square-path Sagnac interferometer to apply a moire fringe heterodyne technique and were able to achieve enhanced resolution over previously existing systems. More recently, Sweedler and Denton (27) and co-workers reported the development of a spatial interferometer using a triangular common path Sagnac interferometer. Their system does not consist of any moving parts, and uses a linear charge coupled device (CCD) as the detector. They have analyzed the spectral properties and the characteristics of CCDs and other array detectors used.

All of the interferometers described above obtain the interferogram as a spatial intensity distribution pattern, rather than an intensity distribution as a function of time. This inherent feature of the non-moving parts interferometer can lead to another significant advantage - the spectrum can then be obtained from the interference record by optical processing, rather than computational processing. The interferogram produced in space rather than time, can be optically analyzed using coherent light to produce the constituent spectrum. An alternative to coherent optical processing is presented in this work.

It is seen that a significant cost advantage and an increase in simplicity of design and operation might be expected from the development and use of non-moving parts interferometers. There is ample justification for the development of simple and inexpensive FT-IR instrumentation for certain severe military and environmental applications. This work describes the design and construction, and demonstrates the performance of an interferometer based spectrometer for application in the UV-Vis spectral region with potential for application in the mid-IR spectral region. This novel interferometer design is based on the three mirror Sagnac interferometer (also known as a common path interferometer) and employs a single, simple moving part, and is capable of real time spectral analysis through optical processing of the spatial intensity record. The interferometer is designed with off-the-shelf optical components and employs a single silicon photodiode detector. Optical path difference is achieved by a small tilt of one of the mirrors in the interferometer, and the resultant spatial intensity pattern is optically processed to produce the final spectrum (29).

CHAPTER II

THEORY OF TWO BEAM INTERFERENCE

The scalar three-dimensional differential wave equation for an electromagnetic wave travelling in space and given by

$$\psi = f(x,y,z,t)$$

where **x**, **y** and **z** are the position coordinates and **t** is the time, is

$$\frac{\delta^2\psi}{\delta x^2}+\frac{\delta^2\psi}{\delta y^2}+\frac{\delta^2\psi}{\delta z^2} = \frac{1}{v^2}\frac{\delta^2\psi}{\delta t^2}$$

This is a linear differential equation and therefore any linear combination of individual solutions to this equation will produce another solution. Thus

$$\psi(r,t) = \sum_{i=1}^{n} C_i\psi_i(r,t)$$

(where **r** the is position vector) will satisfy the wave equation. The coefficients C_i are arbitrary constants. This property of being able to produce a solution to the wave equation by a linear combination of individual solutions is called the principle of superposition. Accordingly, the resultant disturbance of a set of individual waves superimposed in space is an algebraic sum of the individual waves. Since the principle of superposition of waves applies strictly only to linear systems, it is necessary to determine if common spectroscopic systems are indeed linear.

An optical system may be termed linear if an increase in the input leads to a proportional increase in the output. In most real systems, the output is modified by the properties of the system through which the input is being processed. These modifications are quite readily quantified and in general have a linear dependence on the input or are constants of the given system and thus render most practical spectroscopic systems linear. However, extremely large input radiation flux density, as in the case of high power lasers, may lead to some non-linear responses from the optical system. In Fourier Transform Spectroscopy (FTS), the radiant flux density incident on a given interferometric system is usually quite low. In fact, it is in the measurement of the spectral characteristics of weak sources of radiation that FTS shows its true advantages over dispersive spectroscopic techniques. Thus, interferometric systems in general may be considered to be linear systems.

Consider two monochromatic point sources S_1 and S_2 emitting waves of the same frequency in a homogenous medium Let the separation a, of the two sources be much greater than their wavelength The point of observation P is located at a distance S such that the wavefronts arriving at P are planes. Considering linearly polarized waves of the form

$$E_1(r,t) = E_{01}\, Cos\, (k_1 \cdot r - \omega t + \epsilon_1) \tag{2.1}$$

and

$$E_2(r,t) = E_{02} \, Cos \, (k_2 \cdot r - \omega t + \epsilon_2) \tag{2.2}$$

where ϵ_1 and ϵ_2 are the initial phases, $\mathbf{k_1}$ and $\mathbf{k_2}$ are the propagation constants, **r** is the position vector, ω is the frequency, and **E** the amplitude of waves 1 and 2 respectively. The irradiance at *P* is given by

$$I = ev\langle E^2 \rangle \tag{2.3}$$

where

e = permittivity of the medium,

v = velocity of the waves in that medium

Considering only the relative irradiances within the medium, we neglect the constants and let

$$I = \langle E^2 \rangle \tag{2.4}$$

where $\langle E^2 \rangle$ is the time average of the square of the electric field intensity. This can also be written as

$$E^2 = E \cdot E \tag{2.5}$$

then

$$E^2 = (E_1 + E_2) \cdot (E_1 + E_2) \tag{2.6}$$

which gives

$$E^2 = E_1^2 + E_2^2 + 2E_1 \cdot E_2 \qquad (2.7)$$

on taking the time average of both sides, we get

$$I = I_1 + I_2 + I_{12} \qquad (2.8)$$

where

$$I_1 = <E_1^2>$$

$$I_2 = <E_2^2>$$

and

$$I_{12} = 2<E_1 \cdot E_2>$$

I_{12} is the interference term. With reference to equations (2.1) and (2.2), we get

$$\begin{aligned} E_1 \cdot E_2 = E_{01} \cdot E_{02}\, Cos(k_1 \cdot r - \omega t + \epsilon_1) \\ * Cos(k_2 \cdot r - \omega t + \epsilon_2) \end{aligned} \qquad (2.9)$$

which is

$$\begin{aligned} E_1 \cdot E_2 = E_{01} \cdot E_{02}\, [Cos(k_1 \cdot r + \epsilon_1) \\ * Cos\ \omega t + Sin(k_1 \cdot r + \epsilon_1)\ Sin\ \omega t] \\ * [Cos\ (k_2 \cdot r + \epsilon_2)\ Cos\ \omega t \\ + Sin(k_2 \cdot r + \epsilon_2)\ Sin\ \omega t] \end{aligned} \qquad (2.10)$$

The time average of a function f(t) taken over an interval T, is given by

$$<f(t)> = \frac{1}{T} \int_t^{t+1} f(t')\, dt' \qquad (2.11)$$

The period for a harmonic function τ, is given by

$$\tau = \frac{2\pi}{\omega}$$

Let $T >> \tau$. Then on simplifying equation (2.10), we get

$$<\boldsymbol{E}_1 \cdot \boldsymbol{E}_2> = \frac{1}{2} (\boldsymbol{E}_{01} \cdot \boldsymbol{E}_{02}\ Cos\ \delta) \tag{2.12}$$

where

$$\delta = (\boldsymbol{k}_1 \cdot \boldsymbol{r} + \epsilon_1 - \boldsymbol{k}_2 \cdot \boldsymbol{r} - \epsilon_2)$$

is the phase difference which has a contribution from both the path-length difference between the light beams emitted from the two sources and the initial phase-angle difference. The interference term is now given by

$$I_{12} = \boldsymbol{E}_{01} \cdot \boldsymbol{E}_{02}\ Cos\, \delta \tag{2.13}$$

Generally, in interferometry we usually deal with the situation in which $\boldsymbol{E}_{01}$ is parallel to $\boldsymbol{E}_{02}$. The irradiance can then be written as the following scalar quantity

$$I_{12} = E_{01} E_{02}\ Cos\, \delta \tag{2.14}$$

Further,

$$I_1 = <E_1^2> = \frac{E_{01}^2}{2}$$

and

$$I_2 = \langle E_2^2 \rangle = \frac{E_{02}^2}{2}$$

and

$$I_{12} = 2\sqrt{I_1 I_2}\cos\delta$$

The total irradiance can then be written as

$$I = I_1 + I_2 + 2\sqrt{I_1 I_2}\, Cos\,\delta \tag{2.15}$$

It is clear that the value of I_{12} determines the resultant irradiance, which is a function of the phase difference δ. The conditions for interference can then be written as follows: total constructive interference is obtained when the phase difference is an even integral multiple of 2π.

This yields a maximum in the irradiance which is given by

$$I_{max} = I_1 + I_2 + 2\sqrt{I_1 I_2} \tag{2.16}$$

Total destructive interference is obtained when the phase difference δ is an odd integral multiple of 2π. This yields a minimum in the irradiance which is given by

$$I_{min} = I_1 + I_2 - 2\sqrt{I_1 I_2} \tag{2.17}$$

The intermediate values of the phase difference yield different levels of constructive and destructive interference. If the amplitudes of both the waves reaching the point of observation are the same ($E_{01} = E_{02}$), as would be the case in an ideal amplitude splitting interferometer, the maximum and minimum irradiances are as follows: since the amplitudes are the same, let

$$I_1 = I_2 = I_0$$

then from eq. 2.15 we get

$$I = 2I_0 * (1+Cos\delta) \tag{2.18}$$

which is equal to

$$I = 4I_0 \, Cos^2\frac{\delta}{2} \tag{2.19}$$

and thus from Eq. 2.16 and Eq. 2.17 we get

$$I_{max} = 4I_0 \tag{2.20}$$

and

$$I_{min} = 0 \tag{2.21}$$

The Fourier integral and the Fourier Transform, which are central to the subject of Fourier Transform Spectroscopy are described in the following section.

The Fourier Integral

Consider a function of the form *F(x)* of the real variable *x*, and another function *f(k)* of the real variable *k* (13). Then *F(x)* is said to be the full Fourier transform of the function *f(k)* if

$$F(x) = \int_{-\infty}^{+\infty} f(k)\, e^{(2\pi ikx)}\, dk. \tag{2.22}$$

This is a Fourier integral and by applying Fourier's inversion theorem we get

$$f(k) = \int_{-\infty}^{+\infty} F(x)\, e^{(-2\pi ikx)}\, dx \tag{2.23}$$

and thus *f(k)* and *F(x)* can be regarded as Fourier transforms of each other and the real variables *k* and *x* will have reciprocal dimensions. The transforms are valid if and only if

$$\int_{-\infty}^{+\infty} |f(k)|\, dk \tag{2.24}$$

and

$$\int_{-\infty}^{+\infty} |F(x)|\, dx \tag{2.25}$$

are finite and definite. Further, *F(x)* and *f(k)* must have only a finite number of finite discontinuities. Under these conditions, *F(x)* and *f(k)* are called a Fourier transform pair.

If *F(x)* is a real function and is symmetrical about the origin, it is an even function and it can be written as $F_e(x)$ and its Fourier transform is given by

$$f(k) = Re \int_{-\infty}^{+\infty} F_e(x)\, e^{(2\pi ikx)}\, dx \tag{2.26}$$

which is

$$= 2 * Re \int_{0}^{+\infty} F_e(x)\, e^{(2\pi ikx)}\, dx \tag{2.27}$$

This is real and is the cosine Fourier transform of $F_e(x)$ (In practice, the prefix "Re" is dropped, with the understanding that this represents the real part of the function, the Imaginary part having gone to zero). Also, since *f(k)* = *f(-k)*, *f(k)* is also even. Thus the cosine Fourier transform of $f_e(k)$ is given by

$$F_e(x) = 2 \int_{0}^{+\infty} f_e(k)\, e^{(2\pi ikx)}\, dk \tag{2.28}$$

If *F(x)* is real and odd and is written as $F_o(x)$, then

$$f(k) = Im \int_{-\infty}^{+\infty} F_o(x)\, e^{(2\pi ikx)}\, dx \tag{2.29}$$

$$= 2 * Im \int_{0}^{+\infty} F_o(x)\, e^{(2\pi ikx)}\, dx \tag{2.30}$$

where "Im" represents the imaginary part of the function. This is an imaginary, odd function, and is given by the sine Fourier transform of $F_O(x)$. Similarly, by inversion

$$F_o(x) = 2*Im \int_0^{+\infty} f_o(k)\, e^{(-2\pi ikx)}\, dk \tag{2.31}$$

For interference effects to be observed the two sources need not be in phase with each other. An initial phase difference between the two sources will result in a slightly shifted but otherwise identical fringe pattern. Thus, a finite and constant phase difference is a prerequisite for interference to be observed. It should therefore be theoretically possible to see interference effects for any kind of light source. Indeed, there are a multitude of experimental results substantiating interference effects with all forms of light sources. But, if interference is to be observed and recorded with reasonable ease and reliability, it is best to work with sources with relatively large spatial and temporal coherence characteristics. Of equal importance is the frequency characteristics of the two sources - their frequencies must be almost the same. Even small frequency differences would result in a time dependent and rapidly varying phase difference which would cause I_{12} (eq. 2.14) to average to zero over the time interval of the detection process. Ideally, the amplitudes of the two interfering beams must be the same. This condition would produce fringe patterns of the greatest visibility and contrast. In reality, the amplitudes of the interfering beams are not the same - they can vary by as much 10%, leading to a deterioration in the quality of the interference fringes observed (1).

Consider the schematic interferometer shown in Fig. 2.1. In this interferometer, the two beams split in amplitude from one source, travel two different paths to the detector (13). These two beams have a net path difference greater than zero. If the interferometer is considered to be ideal in all respects, the two beams arriving at the detector will have an effective phase difference directly proportional to the path difference. Let

$$\sigma = \frac{1}{\lambda} = \frac{\nu}{c} = \frac{\omega}{2\pi c}$$

where c is the speed of light ($2.9998 * 10^8$ m/s)

σ is the wavenumber of the radiation (cm^{-1})

ν is the frequency of the light (Hz)

ω is the angular frequency (rad/s)

λ is the wavelength (nm)

Let $S(\sigma_1)$ be the spectral intensity for the spectral component σ_1 of the source. For a pure monochromatic source $S(\sigma_1)$ is the spectral intensity. Then if x is the path difference in the interferometer, the phase difference is given by $2\pi\sigma_1 x$ and the interference function (eq. 2 15) for this monochromatic source is given by

$$I_{\sigma_1}(x) = 4I_0 Cos^2 \pi \sigma_1 x \tag{2.32}$$

$$= I_{\sigma_1}(x) = 2S(\sigma_1)\ Cos^2 \pi\, \sigma_1 x$$

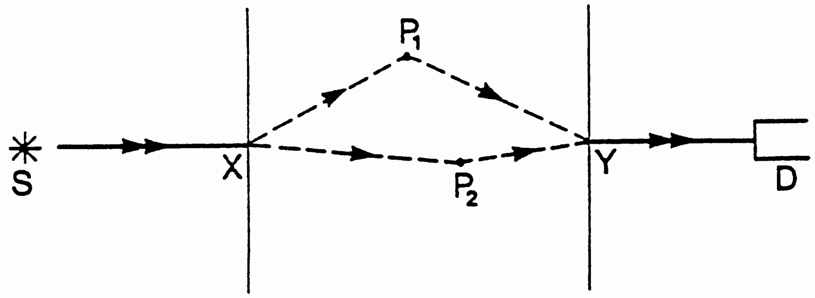

Figure 2 1 Schematic arrangement for a two beam interferometer The radiation from the source S is divided within the interferometer into two partial beams, passing respectively, via P_1 and P_2 These beams recombine before reaching the detector, with a relative phase delay determined by the path difference XP_1Y-XP_2Y within the interferometer (Reproduced from page 6 of "The Principles of Interferometric Spectroscopy" by Chamberlain, J , copyright 1979) and further, by trigonometric identity,

$$I_{\sigma_1}(x) = S(\sigma_1)(1 + Cos 2\pi \sigma_1 x)$$

Thus, for each spectral component in the source of intensity $S(\sigma)$ in the interval σ to $\sigma + d\sigma$, the intensity at the detector is given by

$$I(x) = S(\sigma) d\sigma + S(\sigma) Cos\ 2\pi \sigma x\ d\sigma \tag{2.33}$$

where it is assumed that the contribution from each portion of the amplitude-split beam is the same. For a spectral source with a broad bandwidth, such as is commonly used in spectroscopy, the detected intensity at the detector is given by adding all the individual spectral components (including for the sake of mathematical completeness, the range of all negative frequencies) given by Eq. 2.33. This gives

$$I(x) = \int_{-\infty}^{+\infty} S(\sigma) d\sigma + \int_{-\infty}^{+\infty} S(\sigma) Cos\ 2\pi \sigma x\ d\sigma \tag{2.34}$$

Then, since

$$I(0) = \int_{-\infty}^{+\infty} S(\sigma) d\sigma \tag{2.35}$$

when the path difference x is 0, we get

$$I(x) = I(0) + \int_{-\infty}^{+\infty} S(\sigma)\ Cos 2\pi \sigma x\ d\sigma \tag{2.36}$$

This is the form of the function that describes the variation of the detected spectral intensity at the detector as a function of the path difference x. Eq. 2.36 consists of a part $I(0)=I$ which does not vary with the path difference x, and a variable part which is a function of the path difference x. Although the invariant portion of the function may be factored out, for the sake of completeness it is usually retained. This shows that the measured interferogram is represented by a portion that is variable with the path difference superimposed on a path-difference invariant term. To maintain consistency with present standards, this format will be used in this study. Thus, the expression for the interferogram is given by

$$I(x) = \int_{-\infty}^{+\infty} S(\sigma)\ (1+Cos2\pi\sigma x)\ d\sigma \tag{2.37}$$

This can be written as

$$I(x) = 2\int_{0}^{\infty} S(\sigma)\ (1+Cos2\pi\sigma x)\ d\sigma$$

due to the symmetry of even functions. It is seen that the interferogram depends on the spectrum according to a cosine Fourier integral. Then, by the Fourier inversion theorem, the spectrum of the source is related to the interferogram, also by a cosine Fourier integral given by

$$S(\sigma) = \int_{0}^{\infty} I(x)\ (1+Cos\ 2\pi\sigma x)\ dx \tag{2.38}$$

This shows that the spectrum of a given source may be calculated by Fourier transformation of the measured interferogram. Equations 2.37 and 2 38 are the fundamental equations of Fourier transform spectroscopy.

The Ideal Two Beam Interferometer

In an ideal two beam interferometer, radiation from a point source is collimated by a perfect collimating lens and is amplitude split at a perfect beam splitter. The two amplitude split beams which are equal in amplitude, proceed to the mirrors within the interferometer and then retrace their path to the beam splitter where they are split again. One of the recombined beams is directed back to the source while the other is directed towards a detector through ideal, loss free optics. This results in an interference pattern in the focal plane of the focussing lens. This interference pattern is a function of the phase delay, which in turn is a function of the path-difference between the two beams within the interferometer. This interference pattern is detected by the detector and the variation of the detected power with the phase difference is called the interferogram. The interferogram contains all the spectral information about the incident radiation. Fourier Transform Spectroscopy (FTS) deals with the generation, observation, detection, and analysis of this interference pattern.

Étendue

The existence of an ideal interferometer is purely theoretical There are several physical reasons due to which an ideal interferometer would not function practically. Firstly, one of the primary requirements in an ideal interferometer, the point source, would not deliver a finite and measurable quantity of radiant energy. Thus a practically realizable interferometer must contain a source of finite size. The light gathering power, or throughput of an interferometer with a source of finite size is characterized in terms of its *étendue* (11). This is particularly important when a given interferometer is used for the spectral analysis of faint radiation source. The étendue of a given interferometer is an invariant for the specific arrangement that it is calculated for. Fig. 2.2 shows an arrangement in which the calculation of the étendue for a given interferometer is outlined. The effective areas A_S and A_D of the source and the detector are images of each other. These images subtend the same solid angle at the lenses L_S and L_D , the collimating lens and the focusing lens respectively. If f_s and f_d are the focal lengths of the collimating lens and the focussing lens respectively, then the solid angle is given by

$$\Omega = \frac{A_S}{f_S^2} = \frac{A_D}{f_D^2} \tag{2.39}$$

The amount of radiation accepted by the lens L_S is proportional to the area of the source and the solid angle Ω_S subtended by the lens L_S at a point in the source. This is also true for the amount of radiation reaching the detector, which is proportional to the product of the area of the detector and the solid angle Ω_D subtended by it at a point in it by the lens L_D For a given beam size (extent), since the two lenses L_S and L_D have the same effective area A,

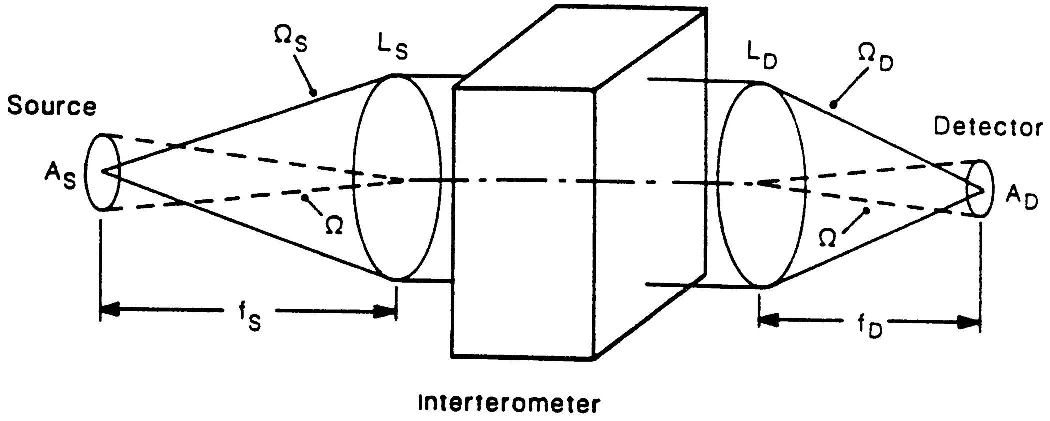

Figure 2.2 Etendue of an interferometer (Reproduced from page 168 of "Optical Interferometry" by Hariharan, P, copyright 1985)

$$\Omega_S = \frac{A}{f_S^2} \tag{2.40}$$

and

$$\Omega_D = \frac{A}{f_D^2} \tag{2.41}$$

and therefore,

$$A_S\Omega_S = A_D\Omega_D = A\Omega = E \tag{2.42}$$

where E is the étendue of the interferometer.

Derivation of the Ideal Interference Function

For a given source, the signal that is detected at the detector is comprised of the individual spectral components of the source, added together algebraically. Each Fourier component of the signal may be considered independently of every other component. Thus the overall intensity from a polychromatic source can be determined by calculating the resultant complex spectral amplitude, finding its absolute value, and then integrating this over all frequencies present. For an ideal monochromatic source, the interference function can be written as

$$I(x) = \frac{1}{2}I_0 + \frac{1}{2}I_0 \, Cos\ 2\pi\sigma_0 x \tag{2.43}$$

where x is the path difference in the interferometer. This is in accordance with the general interference function given by eq. 2.37. It is seen that in the ideal case, the x-dependent (path-length or phase dependent) part of the detected power - the interferogram consists of a cosinusoidal variation that extends to infinite positive and negative path differences, superimposed on a constant background $1/2I_0$. The complementary signal that leaves the beam splitter in the direction of the source is given by

$$I(x) = \frac{1}{2}I_0 - \frac{1}{2}I_0 \, Cos \; 2\pi\sigma_0 x \tag{2.44}$$

This shows that in an ideal interferometer, energy is conserved and the sum of the powers going to the detector and back to the source equals the power propagated initially. The peaks and troughs described by the interference function are called fringes. The fringes appearing in the detector plane and the source plane carry equivalent spectral information, although phase shifted by a factor of 2π. In the case of the ideal interferometer with a monochromatic source, all the bright fringes are of equal intensity - including the bright fringe for zero path difference, and all the dark fringes are of zero intensity. Under these conditions, the visibility and contrast of the interference fringes is a maximum. However, this condition is not attainable for a practical interferometer with a quasi-monochromatic or a polychromatic source.

If the source consists of several monochromatic spectral lines, then by the principle of superposition, the detected power is given by the sum of the contributions of each spectral component separately. Then if the power from the i th line is I_i, we get

$$I(x) = \frac{1}{2}\sum_i I_i + \frac{1}{2}\sum_i I_i \, Cos\; 2\pi\sigma_i x \qquad (2.45)$$

This can now be generalized to give the interference function for a real case, in which even a 'monochromatic' source really has a continuous spectral distribution. Thus I_i the spectral power radiated at wavenumber σ_i, can now be replaced by the power radiated between the spectral region $\sigma \; d\sigma$. This is given by $S(\sigma)\, d\sigma$ and then the total detected power is given by

$$I(x) = \frac{1}{2}\int_0^{+\infty} S(\sigma)\, d\sigma + \frac{1}{2}\int_0^{+\infty} S(\sigma)\, Cos\; 2\pi\sigma x \, d\sigma \qquad (2\,46)$$

which is the same result given by eq. 2.13. The power returning to the source is now given by

$$I(x) = \frac{1}{2}\int_0^{+\infty} S(\sigma)\, d\sigma - \frac{1}{2}\int_0^{+\infty} S(\sigma)\, Cos\; 2\pi\sigma x \, d\sigma \qquad (2.47)$$

It is now seen that interference fringes given by the second term in the above equations no longer have equal contrast. For zero path difference *$(x=0)$*, there is a bright fringe in the detector plane. This fringe represents a maximum - complete constructive interference for all the spectral components of the radiation source.

This represents the basic equation for FTS with an ideal interferometer irradiated with a collimated point source. In any practically realizable interferometer, this equation must be modified to account for the finite size of the source, the losses due to the optics of the interferometer, and the specific method and factors used to generate the path difference in the Sagnac interferometer (13).

The Sagnac Interferometer

Traditional FTS methods use a mechanical delay between the two arms of an interferometer to introduce a phase shift in the light beams that varies with delay. By contrast, the same information as generated by the positional delay of Michelson type arrangement may be displayed as a lateral variation in intensity in the less commonly used Sagnac interferometer. There are two basic types of Sagnac interferometers - the two mirror type and the three mirror type (11). There are significant differences between the two types and each type has a set of specific applications for which it is best suited. The three mirror Sagnac interferometer also known as the square path Sagnac interferometer was used in this study. The interferometer consists of three plane mirrors arranged to form three sides of a square. A beam splitter is placed perpendicular to the plane of the central mirror. The incoming radiation is split in amplitude by this beam splitter and each of the split beams proceed to each of the two mirrors where they undergo reflections

Fig. 2.3a shows the arrangement of the optical components for the two mirror Sagnac interferometer, and Fig. 2.3b shows the arrangement of the optical components for the three mirror Saganc interferometer. The arrangement with two mirrors has an even number of reflections and the wavefronts within the interferometer are always superposed. In the three mirror Sagnac interferometer, the wavefronts are laterally inverted with respect to each other within the interferometer. This makes it possible to achieve a physical separation of the two beams by a lateral displacement of the incident beam. This property of the three mirror Sagnac interferometer increases its applicability to practical systems. However, it is the insensitivity to lateral displacements of the mirrors and the beam splitter that is of greatest importance in the present study. Significantly, location of FTS field devices on remotely piloted vehicles requires design considerations which minimize sensitivity to vibrations. Thus the insensitivity to vibrations of the three mirror Sagnac interferometer was the primary consideration in its application in this study. Although this interferometer is insensitive to lateral displacements of its mirrors and beamsplitter, any rotation of any of the components about a vertical axis introduces a shear and a corresponding path difference in the two beams within the interferometer. As shown in Fig. 2.4, in the three mirror Sagnac interferometer, light from the source is roughly collimated by the collimating lens L_1 and is incident on the beamsplitter, BS. One part of this amplitude split beam is transmitted through to mirror M_3 and the other part is reflected on to mirror M_1. The reflected and transmitted beams suffer reflections at M_1 and M_3

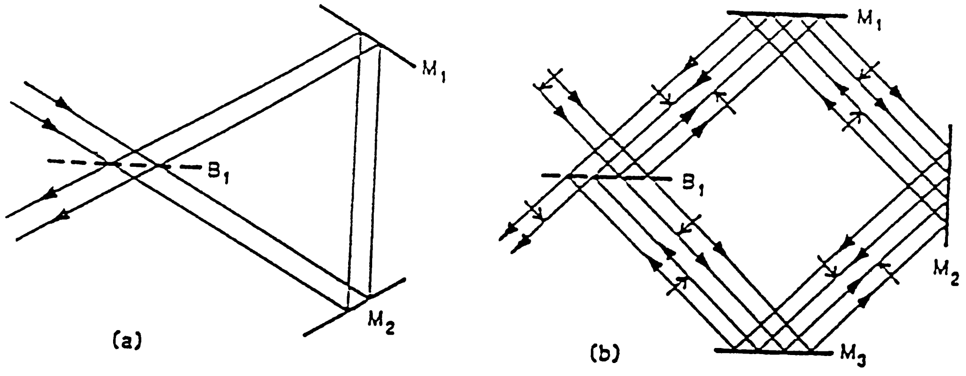

Figure 2.3. Two types of Sagnac Interferometers (Reproduced from page 30 of "Optical Interferometry" by Hariharan P, copyright 1985).

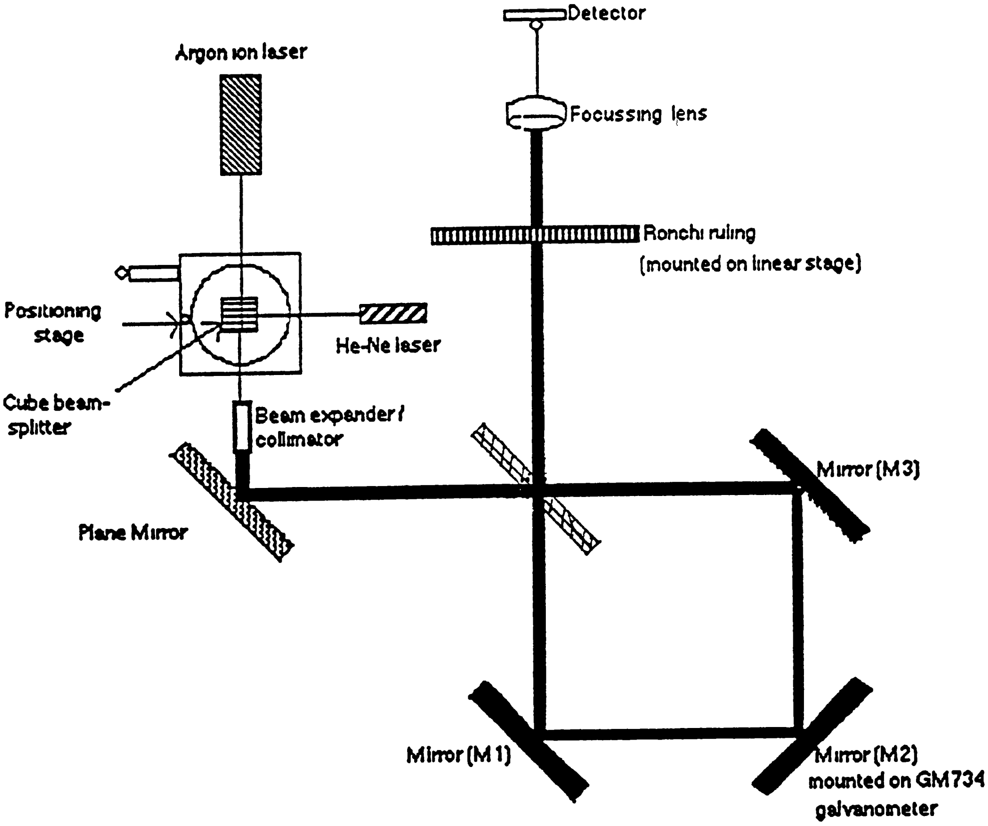

Figure 2 4 Schematic diagram of experimental setup (not to scale) respectively and are brought together in the plane of mirror $\mathbf{M_2}$. Mirror $\mathbf{M_2}$ is mounted such that it can be tilted from its nominal 45° position about a vertical axis. When this is done, the corresponding wavefronts travelling in opposite directions within the interferometer exit at a slight angle to each other, giving rise to wedge fringes in the output beam. For an extended source, the lateral separation of these two beams falls to zero at $\mathbf{M_2}$ and the fringes are localized at the surface of this mirror.

The formation of fringes in the Sagnac interferometer is governed by the type of the radiation source. Fringes can be classified into *real* and *virtual* fringes. Further, both real and virtual fringes can be *localized* or *nonlocalized* (8). Real fringes and virtual fringes have one key difference - the real fringes can be visualized without the use of an additional focusing system, while the virtual fringes cannot be visualized without the use of an additional focusing system. Nonlocalized fringes are real and exist everywhere within an extended three dimensional region of space. Nonlocalized fringes are generally produced by small sources. Localized fringes can be clearly observed only over a definite region of space. Localized fringes are always formed with the use of an extended source, but they can also be formed by point sources.

A point source cannot be used to form virtual fringes that can be directly visualized by the human eye since the human eye can intercept only those rays that are directed to it. Zajac *et al* (30) have constructed a Sagnac interferometer and have shown that under appropriate conditions, both virtual and real fringes are possible with this type of interferometer and that extended sources can be used to form both real and virtual fringes.

The formation of fringes, which is a manifestation of the interference process, is a function of the path difference that is generated between the two beams in a two beam interferometer. In the Michelson interferometer, the path difference is achieved by a lateral translation of the movable mirror. However, in the Sagnac interferometer, the path difference is achieved by a small tilt about the vertical axis of any one of the mirrors that form the interferometer. This introduces a small misalignment of the mirrors from their nominal position and thus produces beams of varied paths proceeding in the clockwise and counterclockwise directions in the interferometer. If the nominal position is such that all the mirrors are inclined exactly at 45° to the sides of a rectangle, no fringes will be observed.

Fig. 2.5a shows the formation of real fringes with a point source in an interferometer with inclined mirrors, such as the Sagnac interferometer, and Fig. 2.5b shows the formation of real fringes with a point source in an interferometer with parallel mirrors. It is seen that the point source S, which is placed in front of the mirrors is replaced by two virtual sources S_1 and S_2. It is seen that only a single ray can be drawn from each of the virtual sources to any point P on the screen. The paths of each of these rays are given by SM_1P and SM_2P and the path difference between the two rays is given by S_2N. (In the three mirror Sagnac interferometer used here, this path difference will be a function of the dimensions

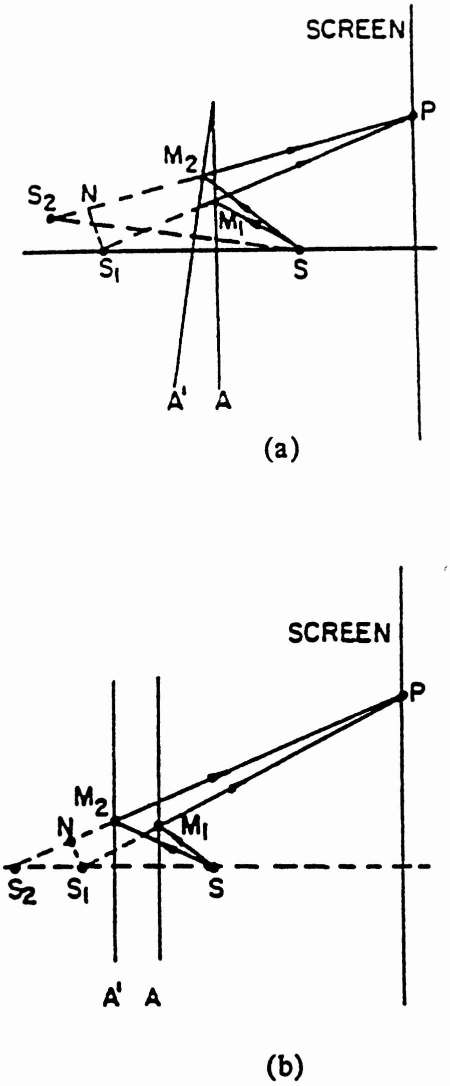

Figure 2.5 Formation of real fringes with a point source for (a) inclined mirrors and (b) parallel mirrors

of the interferometer and the angle of tilt of the moving mirror. This is shown to be the case in the next section). Thus, constructive interference occurs when

$$S_2N = n\lambda$$

and is true only for the case when the net phase change for each beam resulting from various surface reflections is the same. In this case fringes are formed throughout space. The formation of real fringes when an extended source is used can be similarly analyzed with the use of a ray diagram Fig. 2.6 shows the formation of real fringes with an extended source in an interferometer of the Michelson or the Sagnac interferometers. From the figure it is seen that a maximum in the intensity at a point P on the screen occurs if

$$S_1S_1' = n\lambda \quad and \quad S_2'N = n\lambda$$

In this case the clarity of the observed fringes depends upon the distance of the screen from an extended source of a given size. The minimum distance from the extended source that is required to observe fringes of reasonable clarity depends on the spatial extent of the extended source, and as the distance of the screen from the source increases beyond the minimum, the clarity of the fringes also increases. The analysis of the formation of the fringes in the Sagnac interferometer shows that these fringes are more stable because both beams traverse the same path, but in opposite directions within the interferometer. Thus any disturbance such as vibrations, will affect all the components of the interferometer

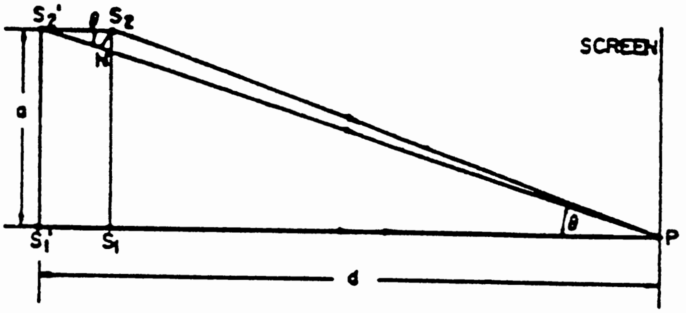

Figure 2 6 Formation of real fringes with an extended source simultaneously, and thus will affect both the beams equally.

Path Difference Generation in the Sagnac Interferometer

As shown in Fig. 2.4, mirror M_2 is mounted such that it can be moved from its nominal 45° position about its vertical axis. This introduces a small difference in the mutual angle of the two counter-propagating beams within the interferometer. This difference in the angle leads to the formation of wedge fringes in the exit plane of the interferometer. In earlier experiments, the movable mirror M_2, was moved away from its rest position and then stopped. The interference pattern generated was recorded and then the mirror was moved to a new position and the new interference pattern was again recorded. In this study, the mirror was mounted such that it could be scanned through a range of angles away from the nominal 45° position.

The expression for the path difference in the three mirror Sagnac interferometer was derived from the basic principles of interference. The derivation of this expression is best described by examining the interferometer's physical characteristics. Consider the case in which all the mirrors and the beam splitter in the Sagnac interferometer are at their nominal position. In this case, the interferometer is perfectly aligned and the net path difference between the two counter-propagating beams is zero. No interference is observed, and the output of the interferometer produces no fringes. Now, if mirror M_2 is tilted by a small angle θ, the beam propagating in the clockwise direction is reflected from mirror

$\mathbf{M_2}$ at an angle 2θ. This beam proceeds to mirror $\mathbf{M_3}$ at this new angle and then on to the beamsplitter. Similarly, the beam propagating in the counterclockwise direction is reflected from mirror $\mathbf{M_2}$ by the same angle and proceeds to mirror $\mathbf{M_1}$ and on to the beam splitter. The two beams arriving at the beam splitter have travelled separate and different paths, and the resultant path difference, which is a function of the angle of tilt of $\mathbf{M_2}$ leads to the generation of interference fringes in the output of the interferometer. The formation of these wedge fringes is uniquely related to the wavelength of the incident radiation and the path difference at that angle of tilt. The fringes formed are of a specific spatial frequency, which for a given wavelength, change with the angle of tilt of mirror $\mathbf{M_2}$. When the path difference is an integral multiple of the wavelength of the light under consideration, total constructive interference occurs, and a bright fringe is observed. When the path difference corresponds to a half-integral multiple of the wavelength, total destructive interference occurs, and a dark fringe is formed.

It is seen from Fig. 2.7, which is a geometrical equivalent of the optical system used here, that the difference in the distance travelled by the two interfering rays is a function of the position of the point of interference on the plane of observation. The distance travelled by ***ray 1*** is given by **AB+BC**. But it is seen that **AB/BC = Cos 2θ.** Thus **BC = AB/Cos 2θ.** Therefore, the path length for ***ray 1*** can now be written as

$$PL_{(ray1)} = AB\left(1 + \frac{1}{Cos\ 2\theta}\right) \tag{2.48}$$

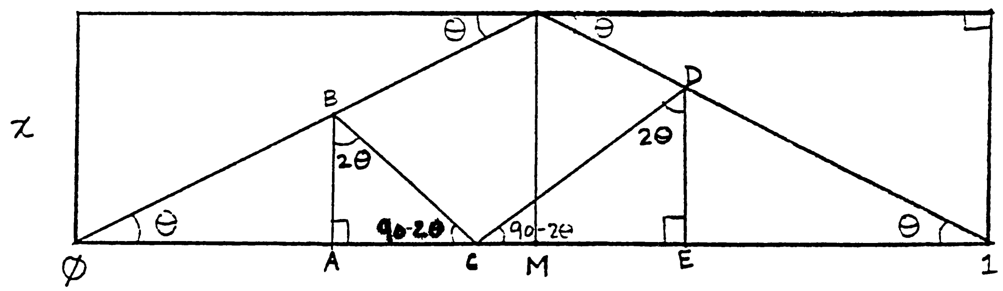

Figure 2 7 Schematic diagram of geometrical arrangement of the interferometer

But in triangle **0BC**, **AB** is the height and is given by

$$\begin{aligned} AB &= \frac{0C}{Cot\theta + Cot(90-2\theta)} \\ &= \frac{0C}{Cot\theta + Tan(2\theta)} \end{aligned} \tag{2.49}$$

Thus the path length for ***ray 1*** can now be written as

$$PL_{(ray\ 1)} = \frac{0C}{Cot\theta + Tan(2\theta)} \left(1 + \frac{1}{Cos(2\theta)}\right) \tag{2.50}$$

A similar analysis shows that the path length for ***ray 2*** can be written as

$$PL_{(ray\ 2)} = \frac{C1}{Cot\theta + Tan(2\theta)} \left(1 + \frac{1}{Cos(2\theta)}\right) \tag{2.51}$$

Now, the optical path difference between ***ray 1*** and ***ray 2*** can be written as

$$\Delta = OPD = \left(\frac{1}{Cot\theta + Tan(2\theta)}\right) \left(1 + \frac{1}{Cos(2\theta)}\right) (C1 - 0C) \tag{2.52}$$

But, **C1 = 01 - 0C** and **01 = 2(0M)**, and **0M = X/Tan θ**, therefore the path difference can now be written as

$$\Delta = \left(\frac{1}{Cot\theta + Tan(2\theta)}\right) \left(1 + \frac{1}{Cos(2\theta)}\right) \left(2\left(\frac{X}{Tan\theta} - 0C\right)\right) \tag{2.53}$$

Equation 2.53 defines the path difference between two interfering beams as a function of the position along the horizontal axis in the plane of observation, as derived for the specific arrangement of the three mirror Sagnac interferometer used here. This equation is exact as written, in that no assumptions regarding the angles have been made. If the angle of tilt of the mirror M_2 is kept very small, the small angle approximation may be used without any significant loss in accuracy (the small angle approximation has not been used here). If the frequency of the input radiation is expressed in units of cm^{-1}, then in equation 2.53, all distances will be represented in cm and all angles will be represented in radians.

For a single frequency $\sigma (cm^{-1})$ of arbitrary intensity $S(\sigma)$, the interference function for the formation of the spatial interferogram in the plane of observation of the interferometer is then given by

$$I(x) = S(\sigma)\,(1 + Cos\,(2\pi\Delta\sigma)) \tag{2.54}$$

where Δ is the Optical Path Difference in the plane of observation, as given by Eq. 2.53.

The spatial interferogram obtained at the exit plane of the interferometer was made incident on the front surface of a suitably positioned Ronchi ruling (31-33). (The Ronchi ruling is a grating with alternating opaque and transparent lines, with the spacing between the lines equal to the width of the lines with the overall transmission of the ruling being 50%) The result of imaging the output of the interferometer on the Ronchi ruling was the formation of Moiré fringes at the

Ronchi ruling, with a spatial frequency equal to the difference between the grating and interferogram frequencies. In the plane of the Ronchi ruling, these fringes appear aligned in the vertical direction, i.e. perpendicular to the optical axis and parallel to the grating lines, and these are particularly obvious when a source with just one or two wavelengths (such as a laser) is used. The transmitted intensity was thus given by this spatial intensity distribution function multiplied by the function representing the Ronchi ruling.

Mathematically, the transmittance of any infinite 2-D periodic grating, whose transmittance profile satisfies the Dirichlet conditions, and which is oriented such that the lines run perpendicular to the horizontal (x) axis, can be represented by the following Fourier series (34)

$$R(x) = \sum_{-\infty}^{\infty} c_n \exp\left(\frac{2\pi n x}{T}\right) \tag{2.55}$$

where T is the period of the grating and the c_n are the complex coefficients of the Fourier series of the 1-D transmission profile along the x-axis. If the profile of the grating $R(x)$ is a square wave, the c_n

will be given by

$$c_n = h\,sinc(nh)\ ;\ where\ sinc(x) = \frac{\sin(\pi x)}{\pi x} \tag{2.56}$$

and in the above equation, h is a fraction of the period that is transparent. If the value of h is exactly 0.5, the grating is called a Ronchi ruling. (Fig. 2.8 shows the theoretically modelled Ronchi ruling with a spatial frequency of 0 0125 cm. This

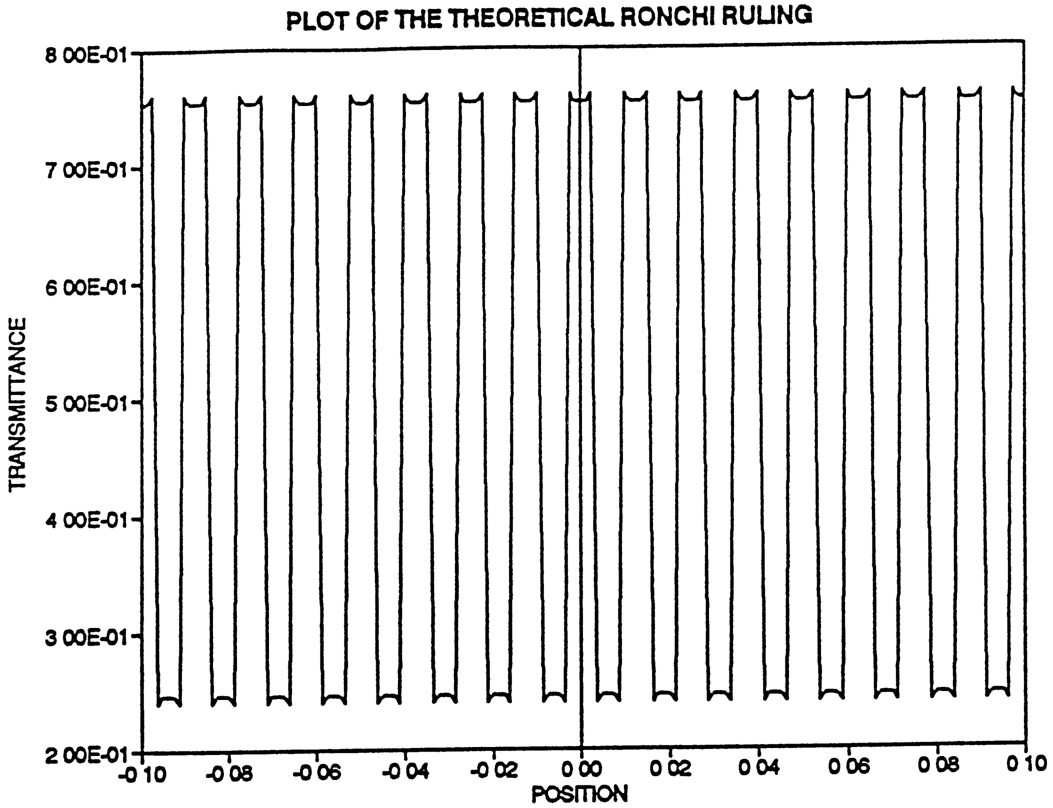

Figure 2 8 Representation of the Ronchi ruling derived from actual physical parameters.

was obtained by plotting the Fourier series representing the Ronchi ruling as a function of the position along the axis perpendicular to the rulings).

As the angle of tilt of mirror M_2 is varied, the frequency and spacing of the Moiré fringes also varies. For a particular value of the tilt angle, and at a given frequency of the incident radiation, the spatial frequency of the Moiré fringes exactly equals the spacing of the Ronchi ruling, and the total intensity at that wavelength is incident on the detector. For a polychromatic source, as the angle of tilt of the mirror M_2 is continuously varied, the spatial frequency of the fringes from different wavelengths will converge upon the spatial frequency of the Ronchi ruling and be transmitted optimally through the grating.

The functioning of the interferometer and the optical spectral analysis system may now be represented by a single Fourier integral, which while consistent with the general theory of Fourier transform spectroscopy, is unique to the experimental system studied here. This expression, as derived here, may represented as follows:

$$S(\sigma) = \int_0^1 I(x) \; R(x) \; dx \tag{2.57}$$

where

$S(\sigma)$ is the spectrum of the source as detected at the detector, and

$$I(x) = \int_{\sigma_1}^{\sigma_2} S(\sigma) \, (1 + Cos(2\pi \Delta \sigma) \, d\sigma$$

and

$$R(x) = \sum_{-\infty}^{\infty} c_n \, Cos\left(\frac{2\pi n x}{T}\right)$$

with

$$c_n = h sinc(nh) \; ; \; where \; sinc(x) = \frac{\sin(\pi x)}{\pi x}$$

Eq.2.57 is the expression for the acquisition of a spectrum of a polychromatic source in the frequency range between σ_1 cm^{-1} and σ_2 cm^{-1}, with the interferometer described here. This equation has three components - the spatial interferogram represented by *I(x)*, the Fourier transformer represented by *R(x)* (the Ronchi ruling), and the integration from 0 to 1 representing the integration of the transmitted intensity over the area of the focussing lens. This expression describes completely the process of the formation of the Moiré fringes and the subsequent inverse transformation of the spatial interference record to produce the recorded spectrum.

Further, Eq. 2.57 provides the fundamental basis for the calculation of all the theoretical spectra presented in this work. The procedure employed in the calculation of the spectra is presented in the experimental section and the actual theoretical spectra are presented in the results section of this thesis.

CHAPTER III

EXPERIMENTAL DETAILS

Design and Construction of the Interferometer

Optical Components of the Three Mirror Sagnac Interferometer

A Melles-Griot (35) model 03 BSC 005 Beamsplitter Cube was used to combine the output of the two laser sources used here. This beamsplitter cube had dimensions of A=B=C = 12.7 mm. The beamsplitter had a hybrid coating with a transmission range of 400 nm to 700 nm, and consisted of a matched pair of identical right angle prisms cemented together. This beamsplitter had a typical absorption of about 10% with reflection and transmission being about 45% each. The beam expander used to expand the input laser beams was an Oriel Laser Beam Expander/Collimator (36), model 15900. This beam expander uses a Galilean Telescope design with a diverging input lens and a converging output lens. The converging output lens had a 23.00 mm aperture and a 80 00 mm focal length and the diverging input lens had a focal length of -8.00 mm. The input aperture of this lens was 4.00 mm, and when used with the model 15900 Laser Beam Expander/Collimator, provided a magnification factor of 10 This expander/collimator had a useful operational wavelength range between 400 nm and 700 nm. The input lenses were interchangeable, depending on the extent of beam expansion desired. The use of a cemented doublet (or achromat) for the output lens improved image quality with negligible spherical aberration.

The Sagnac interferometer was constructed with square flat mirrors obtained from Melles-Griot (Irvine, CA). These mirrors (model 01 MFG 011) were 50.0 mm x 50.0 mm x 3.0 mm in dimensions and were made of optical crown glass with a protected aluminum coating. The dimensions were accurate to better than ± 0.25 mm. These optical crown glass mirrors had a surface flatness rating of 3λ per 25 mm at 546 nm over the central 90% of the aperture. Cosmetic surface quality was better than 80-50 scratch and dig standard. The protected aluminum coating material has its maximum reflectance of 90% at approximately 550 nm, and has a reflectance of better than 85% in the wavelength region from 400 nm to 750 nm. A mirror of the same specifications was used to direct the input beam into the interferometer. The square plate beamsplitter used to split the amplitude of the input beam in the interferometer was also obtained from Melles-Griot (Irvine, CA). The beamsplitter (model 03 BTF 007) was 50 mm x 50 mm and was 1 mm in thickness. This beamsplitter was made of optical crown glass with a different type of coating on either side. The first surface was coated with an all-dielectric film having partial reflection properties in the visible and near-infrared spectrum. The second surface was coated with a HEBBAR^{TM} broadband antireflection coating optimized for 45°. Fig. 3.1 shows a

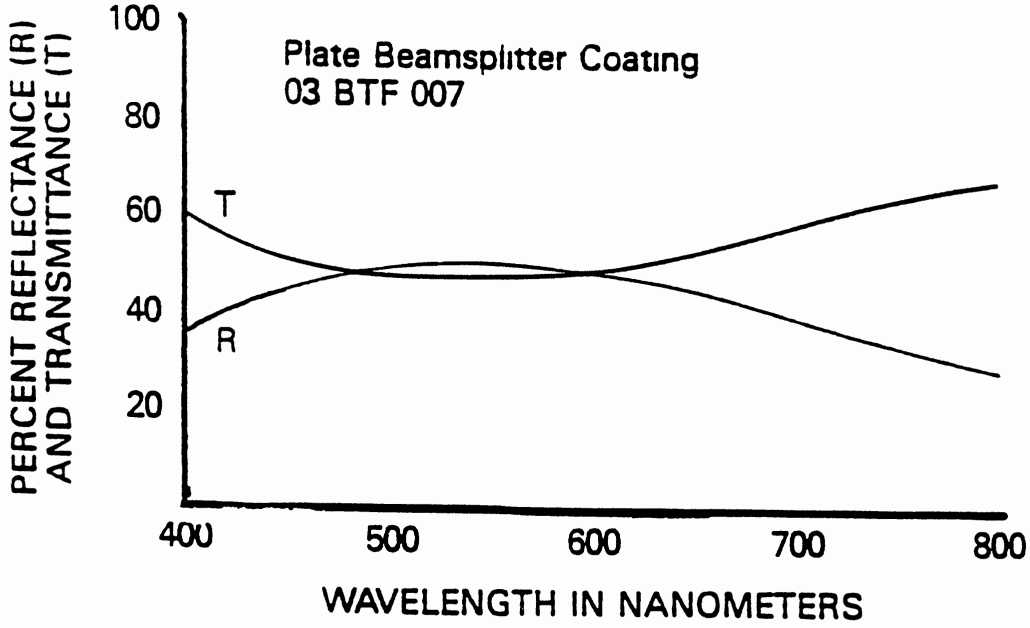

Figure 3 1 Wavelength vs percent reflectance/transmittance curve for plate beamsplitter coating reflectance/transmittance profile for the beamsplitter coating.

The Ronchi Ruling, which is a grating with evenly spaced lines running parallel to each other with the line width equal to the space width next to it was obtained from Edmund Scientific Corporation (Barrington, NJ) (37). The Ronchi Ruling used in this application had dimensions of 2.00" x 2.00" x 0.2", and was made of a glass substrate on which the lines were precision etched and filled with black opaque, with a rule frequency of 200 lines per inch. Ronchi rulings with 500 and greater lines per inch are precision made by evaporating chrome on a glass substrate.

The focussing lens placed between the Ronchi ruling and the photodetector was a Melles-Griot model 01 LAU 144 uncoated achromat. This lens had a diameter of 23.0 mm ± 0.2 mm and a focal length of 60.00 mm. The center thickness of the lens was 8.7 mm ± 0.25 mm, and the edge thickness was 6.0 mm. The lens was made of grade A fine annealed crown glass, with the two elements cemented with Canada Balsam. The transmission range of this lens was from 400 nm to 2.5 μm. The cosmetic surface quality of this lens was better than 80-50 scratch and dig standard.

Mechanical Components

The cube beam splitter used to combine the output of the He-Ne laser and the Ar^+ ion laser was mounted directly on a Newport Research Corporation (Fountain Valley, CA) (38) Model 471 Rotation Stage This was mounted on an anodized optical rail, which was in turn mounted on the optical breadboard with appropriate screws The Model 471 Rotation Stage provided smooth, wobble-free angular motion over 16° of fine adjustment travel. The model 471 Rotation Stage was fitted with a SM-05 Vernier Micrometer, which provided a direct readout proportional to an angular displacement of 76 arc-minutes per millimeter of drive travel. The beam expander/collimator was mounted on a Newport Research Corporation model MB-2 Magnetic Base fitted with an aluminum post and screw type post clamps. The magnetic base was placed directly on the optical breadboard.

Newport Research Corporation gimbal mounts model GM-2 were used to mount the three fixed mirrors used in the interferometer. The mirrors were directly bonded to the mounts using a cyanoacrylate based adhesive. Mounting the mirrors on such a mount allowed for dual axis control. The plate beamsplitter was mounted on a similar mount and was directly bonded to its mount also. Mirror M_2, which could be tilted from its nominal 45° position along an axis perpendicular to the optical axis, was mounted on a Newport Research Corporation model MM-2A mirror mount.

This mirror M_2 and its mount were directly attached to the shaft of a General Scanning Inc., (Watertown, MA) (39) model GM-734 open loop galvanometer, by means of an aluminum rod, 12.5 mm in diameter and 16 mm in length. The length and diameter of this connecting rod was kept to a minimum in order to minimize torsional strain leading to excessive roll, yaw or pitch, while still allowing access to the retaining and adjusting screws.

The individual components of the interferometer were mounted on a Newport Research Corporation XS Series optical breadboard. This 2' x 4' optical breadboard had a ferromagnetic steel skin and unsealed, equally spaced mounting holes with a spacing of 1.00". The mounting holes were all of the same size and were designed to accept standard optical mounting screws. Although the breadboard was no substitute for optical tables, and its size-to-thickness ratio produces relatively low end-to-end rigidity, it had very good local rigidity characteristics. Significantly, over distances of less than 60 cm, the local rigidity of the breadboard was sufficiently high as to warrant its use as a base for the interferometer. Mirrors M_1, M_3, and the beamsplitter, were rigidly mounted at the appropriate angles and distances on an anodized aluminum optical rail, which was then fastened to the optical breadboard by means of appropriate screws. The GM-734 open loop galvanometer, with the movable mirror M_2 - Galvanometer assembly, was mounted independently on to the optical breadboard by means of specially modified fasteners. The Ronchi ruling was directly bonded to a Newport Research Corporation model GM-2 gimbal mount. This was then mounted on a Melles-Griot Linear translation stage. This translation stage had a coarse and fine micrometer adjustment, allowing for the precise positioning of the Ronchi ruling. This linear translation stage was then mounted rigidly on the optical breadboard using specially modified fasteners.

The focussing lens was mounted on a Newport Research Corporation model MB-2 magnetic base fitted with an aluminum post and a suitable lens holder. The lens holder was attached to the aluminum post with a screw type post clamp.

The detector assembly was mounted on a Newport Research Corporation model 270 laboratory jack that was capable of smooth height adjustment. The top mounted plate had an array of tapped mounting holes allowing for precise horizontal positioning of the detector assembly. The laboratory jack was rigidly mounted on the optical bench with appropriate screws.

The entire optical arrangement, including the two laser sources and the detector assembly was positioned on the optical breadboard such that the maximum distance between any two components did not exceed 60 cm, thus keeping within the high short-range rigidity characteristics of the optical breadboard.

The Laser Light Sources

Two laser sources were used to calibrate and test the interferometer during the course of this study. The first laser was a Melles-Griot model 05 LLP 851 Helium-Neon Laser. This laser had a minimum CW power rating of 5.0 mW in the TEM_{00} mode at 632.8 nm. The nominal $1/e^2$ beam diameter was 0.77 mm with a full beam divergence of 1.0 mrad. This laser had a polarization ratio of > 500:1 and a longitudinal mode spacing of 454 MHz The laser had an output power stability variance of not more than ± 2%. This air-cooled laser had an integrated power supply and was operated at 115 V AC, 60 Hz. The laser was mounted on a Newport Research Corporation optical rail, which was then anchored to the optical breadboard with appropriate screws.

The second laser used in this study was a Cyonics/Uniphase Model (40) 2002-10MLL forced air cooled cw Ar^+ ion laser system. This multiline laser had 458.0 nm, 477.0 nm, 488.0 nm, 502.0 nm, and 514.5 nm wavelength output. The maximum output power of this laser was 0.25 W in the TEM_{00} mode. The nominal $1/e^2$ beam diameter was 0.65 mm with a beam divergence of 0.95 mrad. The minimum polarization ratio for this laser was 250:1. The laser had an independent power supply and was operated at 115 V AC, 60 Hz. The laser was operated in the light control mode wherein the optical output power is held constant by the feedback circuit. This mode of operation allowed for high output power stability over both long and short periods of time. Two wavelengths - 458.0 nm and 488.0 nm - were obtained by operating the laser at minimum power, while operation at full power provided all the five wavelengths. The ratio of the powers for the five wavelengths at maximum operational power was 1.0 : 2.25 : 11.78 : 1.37 : 4.46, for 458.0 nm, 477.0 nm, 488.0 nm, 502.0 nm and 514.5 nm respectively. The power of the radiation incident at various points in the interferometer was measured with an ANDO Type AQ-2101 Optical Power Meter equipped with an ANDO Type AQ-2704 Sensor (ANDO Corporation, USA) (41).

The GM-734 Galvanometer

A general Scanning model GM-734 Open Loop Galvanometer was used in this study to scan mirror M_2 about its vertical axis. The model GM-734 Open Loop Galvanometer was a conventional open loop (no position sensitive feedback control was applied) moving coil iron galvanometer that was suitable for low-power, low-cost applications. This galvanometer with a rated life of 10^{10} cycles, was the equivalent of the drive mechanisms used in more conventional Michelson type interferometers. The specifications of the galvanometer are provided in Table 3.1.

In this study, the galvanometer is used to oscillate mirror M_2 in the three mirror Sagnac interferometer, thus introducing a small path difference in the two counter-propagating beams within the interferometer. Thus, the performance characteristics of the device had to be well established experimentally, and its suitability for application in this interferometer assessed. Further, keeping within the overall specifications of the instrument developed during the course of this study, the device had to be compact and have low power consumption.

The Detection System

The detection system used in this study was based on the United Detector Technology (Hawthorne, CA) (42) UDT-451 PHOTOPS solid-state photodetector. This detector is a high speed solid-state photodetector with integrated electronics. This detector contained a built-in, monolithic JFET operational amplifier which

TABLE 3.1

SPECIFICATIONS FOR THE GENERAL SCANNING MODEL GM-734 OPEN LOOP GALVANOMETER

Maximum Excursion Angle (Rotation)	± 15°
Total Error	± 1.5% (P-P)
Torque at Full Excursion	350 g-cm
Rotor Inertia	2.1 g-cm^2
Static Current at Full Excursion	220 ma
Full Excursion Power	1.2 W
Drive Coil Resistance 27	ohms
Weight	335 g
Life Cycles	1 x 10^{10}cycles (minimum)

allowed for low-level measurements with low-noise output under a variety of experimental conditions. The UDT-451 came packaged in a low-cost 8-pin mini-DIP plastic package. The detector had an active surface area of 5.1 mm^2 and a diameter of 2.5 mm. The spectral range of this detector as specified by the manufacturer was from 350 nm to 1100 nm. The peak responsivity of this detector was 0.5 A/W at 850 nm, with a noise-equivalent power (NEP) of 3.51 x 10^{-13}W/ Hz at 10 V bias voltage (see Table 3.2 for technical specifications of UDT-451). The circuit diagram for the detection system is provided in Fig. 3.2. The detector was housed in a metallic enclosure and was mounted on an adjustable base. A stable 9 V DC battery source provided the necessary power for the detector electronics, and a standard BNC terminal facilitated signal acquisition. The AC response of this detector was experimentally determined by monitoring the amplitude response of the UDT-451 to an acousto-optically modulated (in the audio frequency range) beam from a 3 mW CW He-Ne laser. The AC response curve plotted for the detector showed that the detector had a linear response up to about 15000 Hz (Fig. 3.3). This range of linearity is adequate for the experimental requirements of this study in light of the following considerations: all spectra were obtained at a scanning frequency of 14 Hz. If 512 data points (as digitized by the Data 6000) were to be obtained for each spectrum, the sampling frequency would correspond to 7168 Hz. But, according to the Nyquist sampling criterion, the sampling rate must be twice this value if noise and spectral artifacts are not to be "folded" into the region of interest. In

TABLE 3.2

SPECIFICATIONS FOR THE UDT-451 PHOTOPS^{TM} PHOTODETECTOR-AMPLIFIER COMBINATION

Active Surface Area	5.1 mm^2
Active Surface Diameter	0.100 in (2.54 mm)
Peak Responsivity	0.5 A/W at 850 nm
Capacitance	15 pF at 10 V bias voltage
Shunt Resistance	50 MΩ
Dark Current	100 nA at 10 V bias voltage
Noise Equivalent Power (NEP)	$3.6 \times 10^{-13} W/\sqrt{Hz}$ at 10 V bias voltage
Breakdown Voltage	50 V
Operating Temperature Range	0° C to 70° C
Typical Supply Voltage	± 15 V
Typical Input Bias Current	30 pA
Typical Open Loop Gain (DC)	200 V/mV
Input Noise Voltage	25 $nV/\sqrt{Hz}$ at 100 Hz
Input Noise Current	0.01 $pA/\sqrt{Hz}$ at 100 Hz
Packaging	8-pin mini dip, epoxy protected plastic casing

(Source: United Detector Technologies, CA, USA)

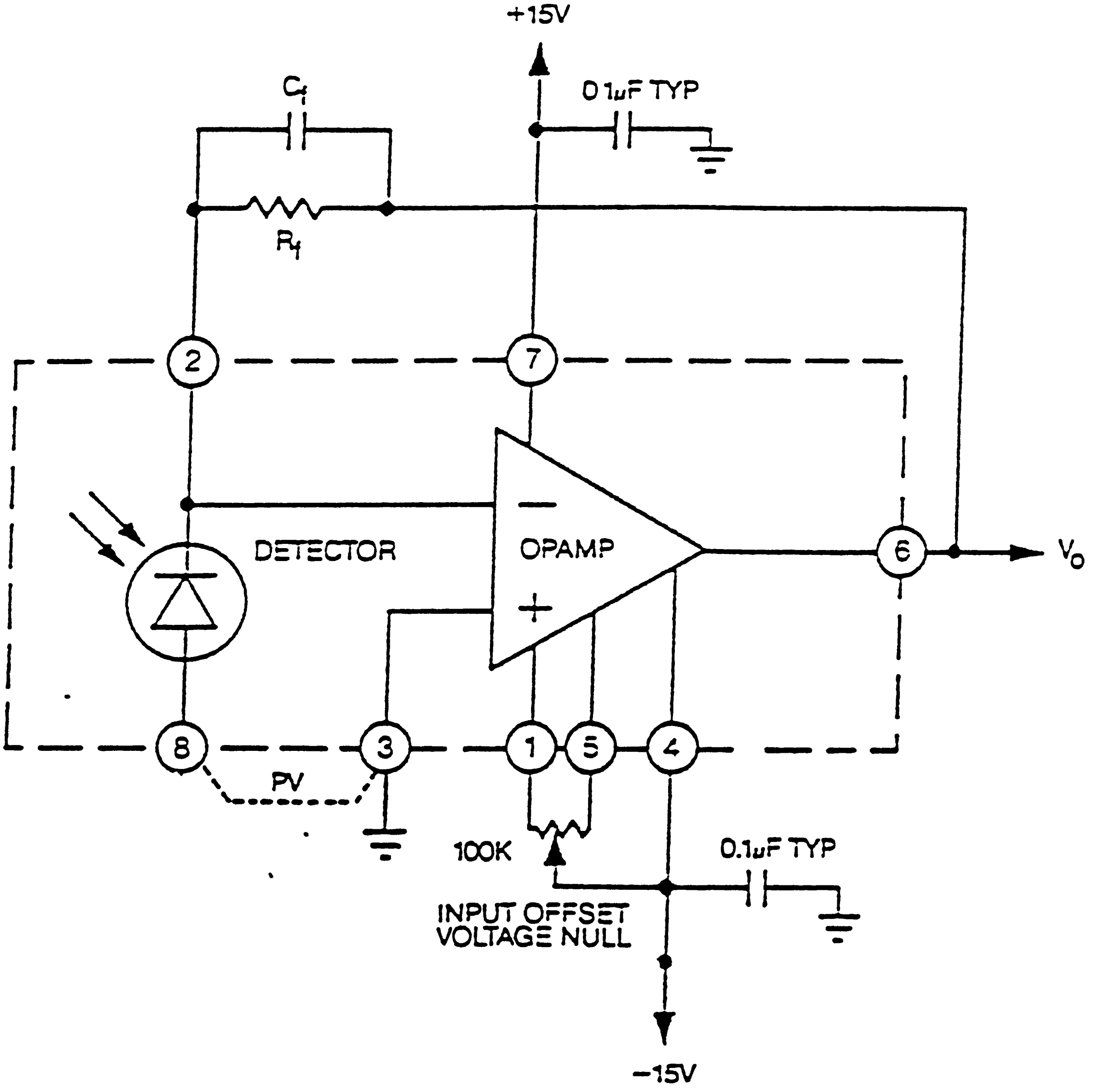

Figure 3 2 Electrical Schematics with external connections shown for United Detector Technology Model UDT-451, PHOTOPS Detector - Amplifier Combination

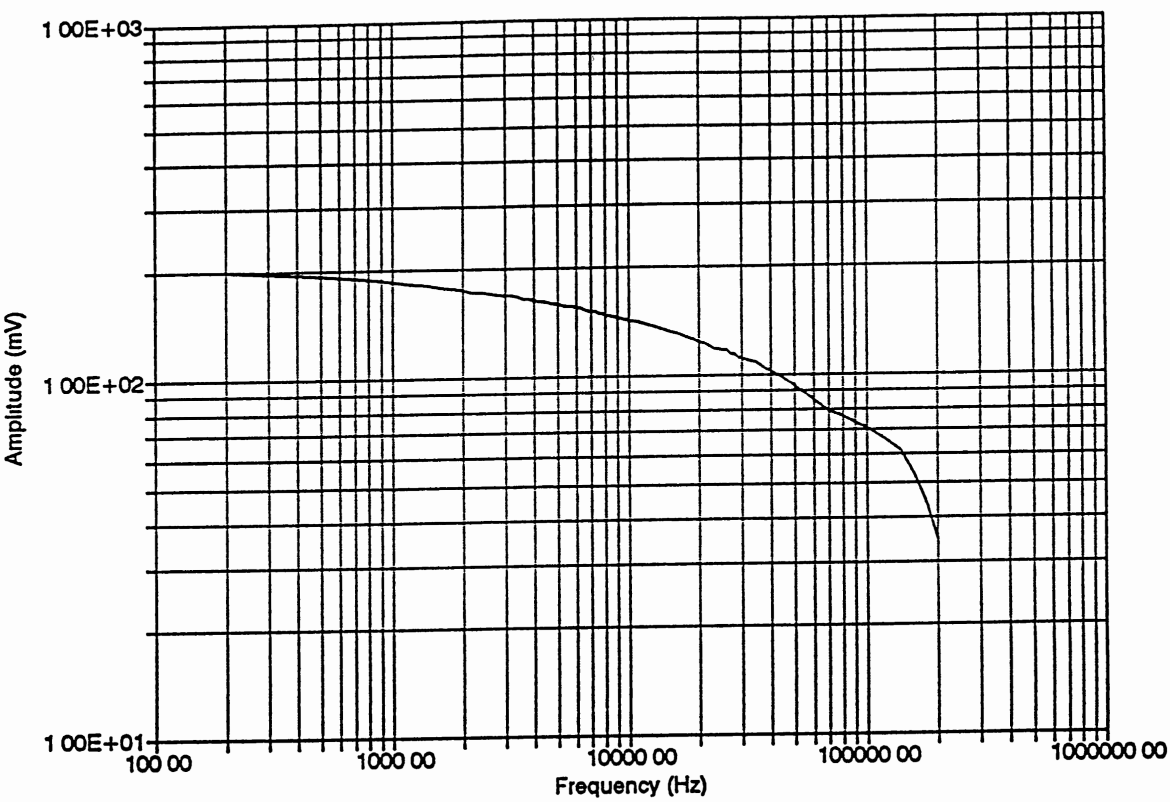

Figure 3 3 Frequency response of the UDT-451 photodetector this case this would correspond to a sampling frequency of 14336 Hz. Thus, the detector must have a linear response at least through this frequency range. The maximum responsivity of the detector (as reported by the manufacturer) was 0.55 Amp/Watt at a wavelength of 850.0 nm. The *Detectivity* (D^*) of the detector was calculated to be

$$Detectivity\ (D^*) = \frac{\sqrt{area}}{NEP} = \frac{0.051\,cm^2}{3.6*10^{-13}\,\frac{Watts}{\sqrt{Hz}}}$$

$$= 1.417*10^{11}\ \frac{cm\sqrt{Hz}}{Watts}$$

Experimental

Spectra were obtained using the general arrangement shown in Fig. 2.4. The Cyonics/Uniphase Ar^+ ion laser was mounted on a Newport Research Corporation (NRC) anodized aluminum optical rail. This rail was then rigidly mounted to the optical breadboard. The air duct (required for cooling the laser) was isolated from the work area so as to reduce the effect of vibrations transmitted from the cooling fan. These vibrations will vibrate the detector, resulting in noise in the observed spectrum, which is an intensity vs time curve. The Melles-Griot He-Ne laser was mounted perpendicular to the beam axis of the Ar^+ ion laser, but in the same horizontal plane. The He-Ne laser was also mounted on a NRC - anodized aluminum optical rail and was rigidly mounted on the optical breadboard. The height of both lasers was carefully adjusted so as to have the beams exiting at very nearly the same height from the top of the optical breadboard. The cube beam splitter, mounted on the precision rotation stage, was placed such that the beam from the Ar^+ ion laser was incident on one of its surfaces, and the beam from the He-Ne laser was incident on an adjacent surface. The distance from the exit port of the Ar^+ ion laser to the cube beam splitter was 7.5 cm and the distance from the exit port of the He-Ne laser and the cube beam splitter was 5.0 cm. This arrangement allowed for the formation of a very nearly collinear output beam from the combination of the output beams of the Ar^+ ion laser and the He-Ne laser. The rotation stage on which the cube beamsplitter was mounted was carefully adjusted to provide an almost collinear output beam.

The output from the lasers was directed into the input lens of the beam expander/collimator. The distance from the cube beam splitter to the input port of the expander/collimator was 9.5 cm. The expanded and collimated beam from the beam expander was made incident on a front surface plane mirror placed at an angle of 45° to the incoming beam. The distance from the output lens of the expander/collimator to this mirror was 35.0 cm. This mirror diverted the entire incoming beam into the interferometer. Specifically, the beam reflected from this mirror was made incident on the plate beamsplitter placed 25.0 cm away. The beamsplitter was adjusted to present an angle of exactly 45° to the incoming beam. At this point the input beam was amplitude split by the beamsplitter, with roughly half the amplitude being transmitted on to mirror M_3 and the other half (approximately) being reflected on to mirror M_1. Mirrors M_1 and M_3 were placed exactly 7.5 cm from the beamsplitter. The amplitude split beams incident on mirrors M_1 and M_3 were each reflected on to mirror M_2, which was also mounted exactly 7.5 cm from mirrors M_1 and M_3 (all mirror-to-mirror and beamsplitter-to-mirror distances are as measured from the center of the mounts).

Mirror M_2 and its mount were attached directly to the General Scanning model GM-734 galvanometer. The contact leads of the galvanometer were connected to a 4-pin micro-connector, which was connected to a banana clip adapter attached to a BNC cable. This cable was connected to the 'signal-out' terminal of a Hewlett-Packard (43) Model 3325A Synthesizer/Function generator. The 3325A was adjusted to drive the GM-734 galvanometer and thus mirror M_2 at a given frequency and voltage. The two counter-propagating beams within the interferometer were recombined at the beamsplitter and roughly half the intensity was directed to the Ronchi ruling placed 7.5 cm from the beamsplitter. It is to be noted here that as in other two beam interferometers, there are two equivalent output beams from the three-mirror Sagnac interferometer - one proceeding toward the detector and the other toward the source. The beam proceeding toward the detector, after having traversed the width of the Ronchi ruling was focussed by the focussing lens on to the detector.

The signal obtained at the detector was fed into an Analogic Corporation (44) (Danvers, MA) DATA 6000 Universal Waveform Analyzer. The DATA 6000 consisted of a Main Frame Unit and a model 610 Plug-In module. The mainframe unit had a 16-bit, 8-MHz CPU, and 48K of internal ROM. The model

610 Plug-In was a two channel 100 Kilosamples/Second unit, with a 14-bit A/D converter resolution. The DATA 6000 was capable of digitizing and storing analog input signals and applying an extensive library of pre-programmed analysis functions to the stored data, and displaying the signal and the processed information on a screen.

The DATA 6000 was equipped with a RS232-C serial interface which was used to interface the DATA 6000 to an IBM XT compatible Cordata microcomputer. The interface was accomplished with the use of the Crosstalk, Data Communications Software System (45), and the data obtained from the DATA 6000 was stored on disk for further analysis and presentation.

The ambient temperature in the laboratory was monitored daily and was found to be between 19° C and 21° C. The relative humidity in the laboratory was between 30% and 40%. No special steps were taken to maintain the temperature or the humidity at any fixed values.

Characterization of the GM-734 Open Loop Galvanometer

A galvanometer scanner is a simple motor in which the moving-iron rotor is limited to angular displacements of about ± 15° from the neutral position (46). The rotor is restored to the neutral position by a torsional spring. The torsional spring could either be coiled or straight depending upon the stiffness required in the galvanometer. The shaft of the galvanometer is rigidly attached to the mass of the rotor and is usually encased in a precision bearing assembly to reduce friction. For a given angular acceleration, the driving torque is proportional to the moment of inertia of the rotor assembly and any additional mass attached to the rotor (Newton's second law of motion). Further, since the moment of inertia of a cylinder rotating about its own axis is proportional to the fourth power of the radius, the diameter of the shaft of the galvanometer is kept as small as possible. This maximizes the dynamic frequency response characteristics of the galvanometer.

A galvanometer operates most efficiently when driven at its natural (resonance) frequency. However, operation of the galvanometer at frequencies even slightly removed from the true resonance frequency can often produce large attenuation in the amplitude of oscillation of the galvanometer. This frequency sensitivity requires special consideration in the design of any optical system based on a galvanometer. Many advanced galvanometers offer the capability of monitoring the instantaneous position or velocity of the rotor within the galvanometer assembly by capacitive or magnetic probes Close monitoring of the galvanometer response allows for corrective measures to be adopted which might mitigate some of the undesirable effects of this attenuation in amplitude. This type of feedback control permits the galvanometer to more closely follow the applied driver waveforms ranging in frequency from dc to 1.0 kHz and including sine, square, triangular, and sawtooth waveforms with the operating frequencies ranging from dc to about 200 Hz in the simple moving coil galvanometer (47).

It was observed experimentally that, when driven at or very near the resonance frequency, the galvanometer used here produces a sine waveform output regardless of the type of driver waveform. This experiment was performed by directing the output of the He-Ne laser to the center of the mirror mounted on the galvanometer (mirror M_2), and then the reflected beam was directed to a United Detector Technologies (UDT) UDT LSC 5D Single Axis Lateral Effect Photodetector connected to a UDT 431 X-Y Position Indicator. The UDT 431, when used with the UDT LSC 5D, senses the position of a light spot on the surface of a detector. This detector generated a voltage proportional to the position of the beam center on the detector. As the position of the beam varied, so did the measured voltage. A plot of the X-axis output of the UDT 431 and the applied driver waveform (14.0 Hz, 80.0 mV (p-p)) for the sine, triangular, sawtooth, and square driver waveforms is presented in Fig. 3.4 to 3.7. In all cases the lower trace represents the driver, while the upper trace represents the response of the galvanometer. It is seen from these plots that the response of the galvanometer is sinusoidal in all cases. Further the amplitude response of the galvanometer is highest in the case of the triangular driver waveform. This formed the basis for the choice of the triangular waveform as the driver waveform of choice in this study. Further, when the X-output of the UDT 431 was plotted vs the driver voltage for each of the four driver waveforms at 14.0 Hz, 80.0 mV (p-p), a Lissajous pattern was obtained (Figs. 3.8 to 3.11) which represented the desired angular deflection of the galvanometer vs the observed angular deflection.

An examination of these "hysteresis" curves shows that the square driver

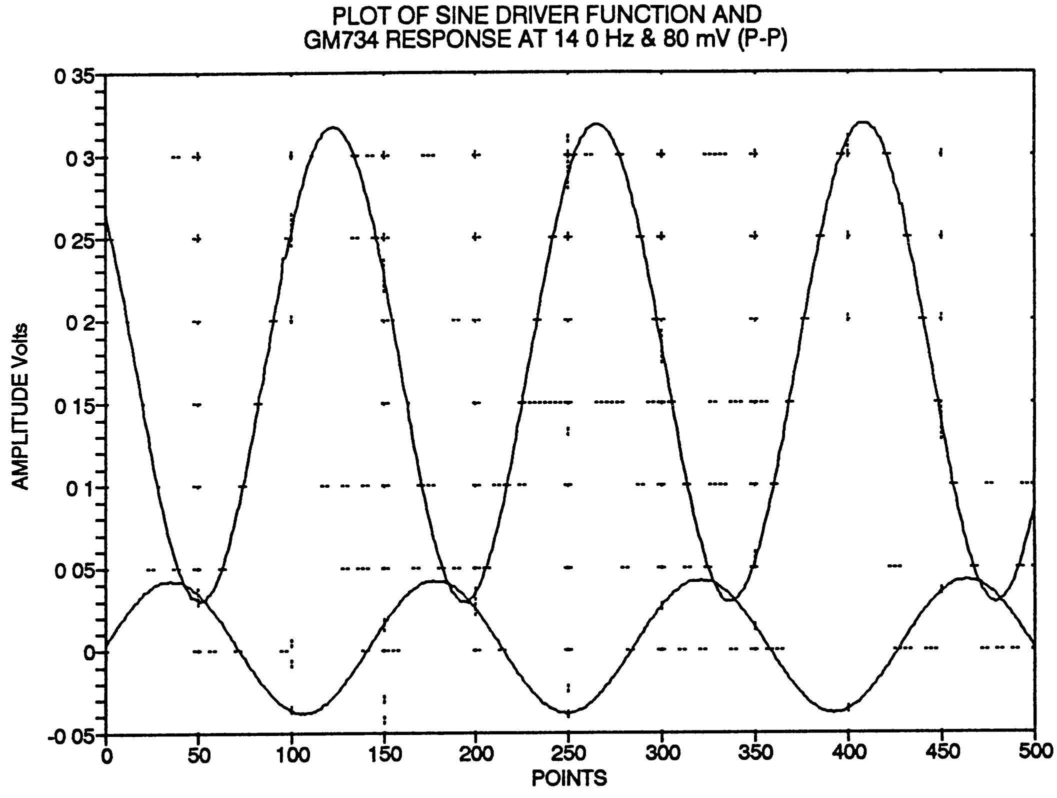

Figure 3 4 Plot of Sine driver function and GM 734 response at 14 0 Hz driver frequency (resonance frequency) and 80 0 mV driver amplitude (P-P) Lower curve is the driver function and the upper curve is the response function

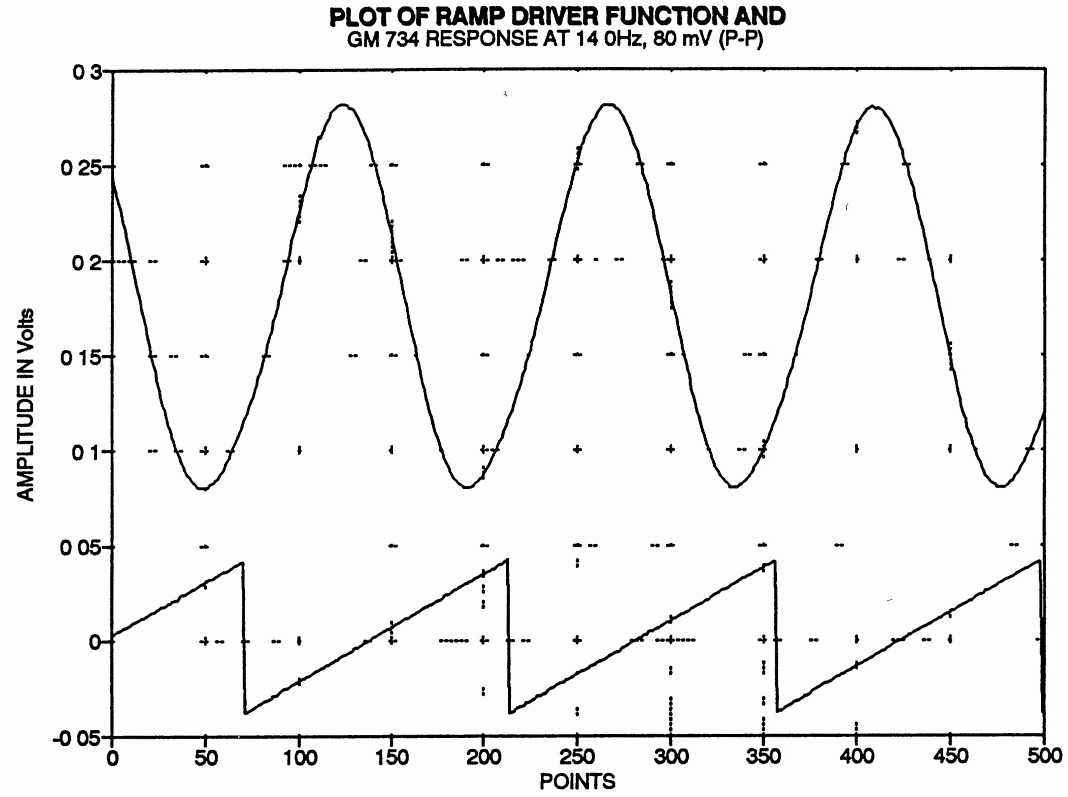

Figure 3.5 Plot of Ramp driver function and GM 734 response at 14 0 Hz driver frequency (resonance frequency) and 80 0 mV driver amplitude (P-P) Lower curve is the driver function and the upper curve is the response function

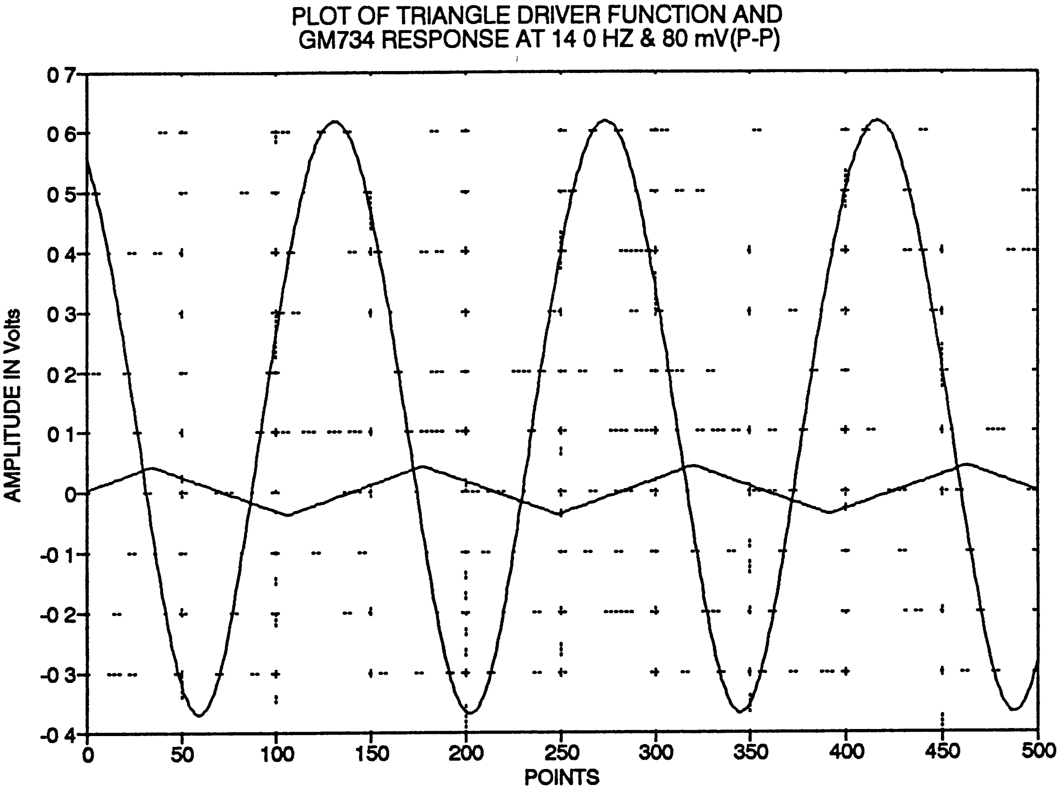

Figure 3 6. Plot of Triangular driver function and GM 734 response at 14 0 Hz driver frequency (resonance frequency) and 80 0 mV driver amplitude (P-P) Lower curve is the driver function and the upper curve is the response function

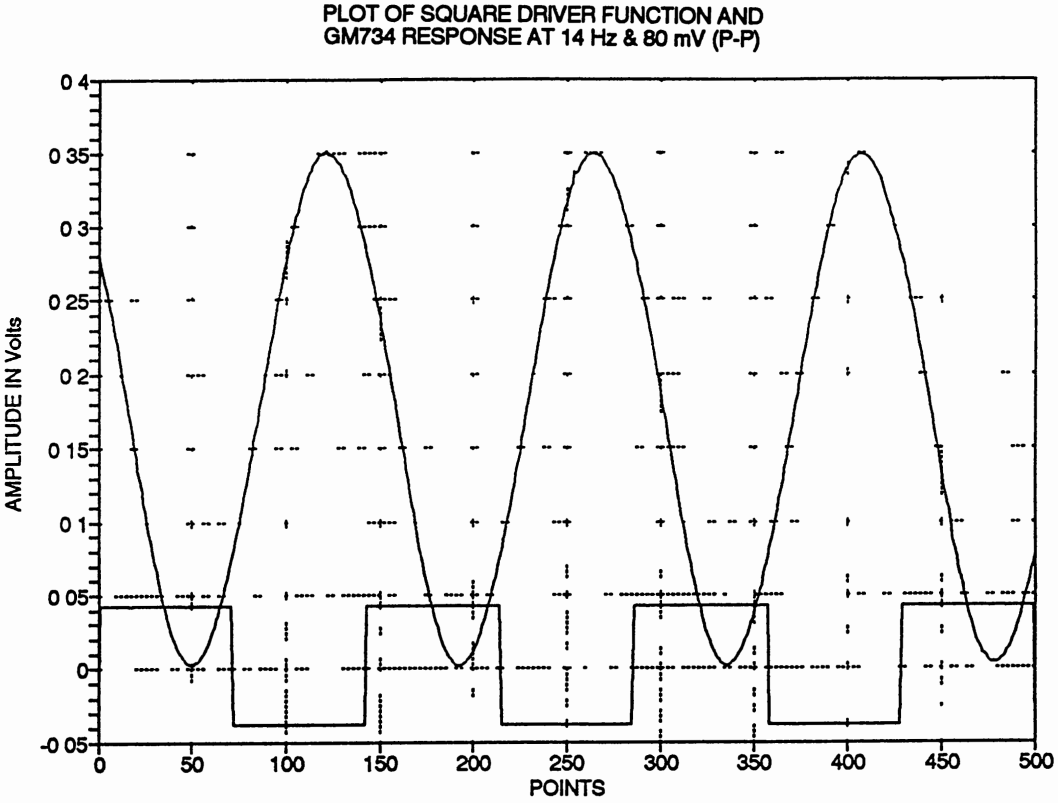

Figure 3 7. Plot of Square driver function and GM 734 response at 14 0 Hz driver frequency (resonance frequency) and 80 0 mV driver amplitude (P-P). Lower curve is the driver function and the upper curve is the response function

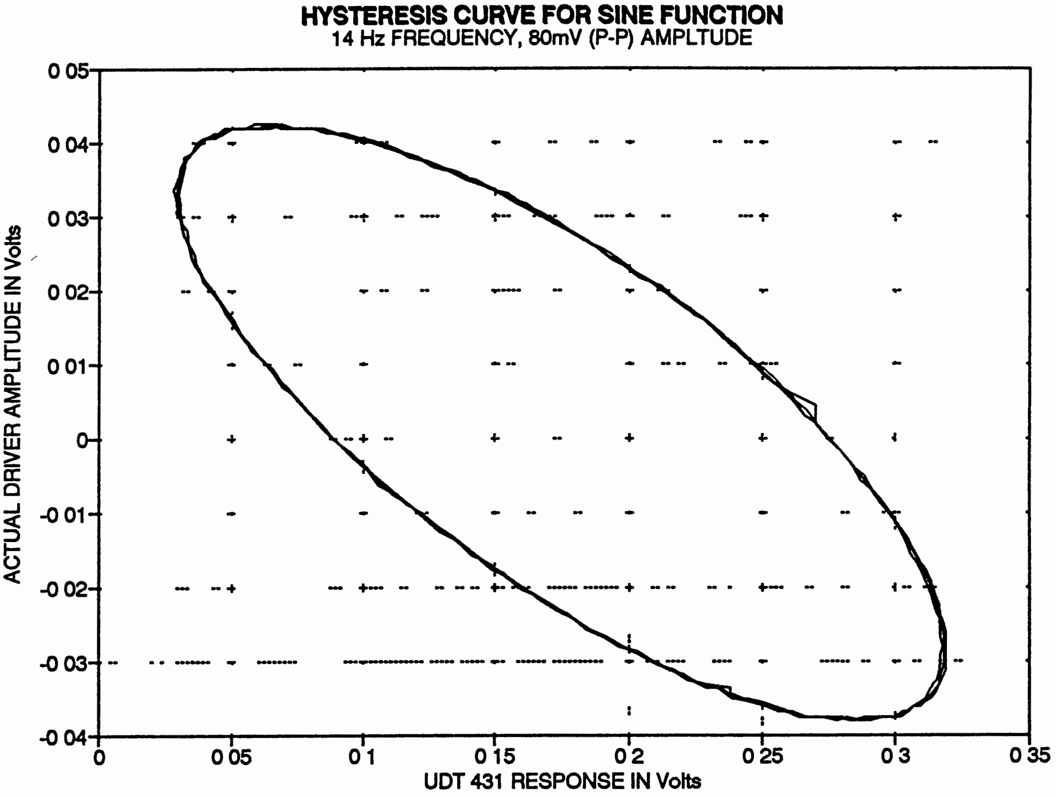

Figure 3 8 Hysteresis curve for Sine driver function at 14 0 Hz driver frequency (resonance frequency) and 80 0 mV driver amplitude (P-P)

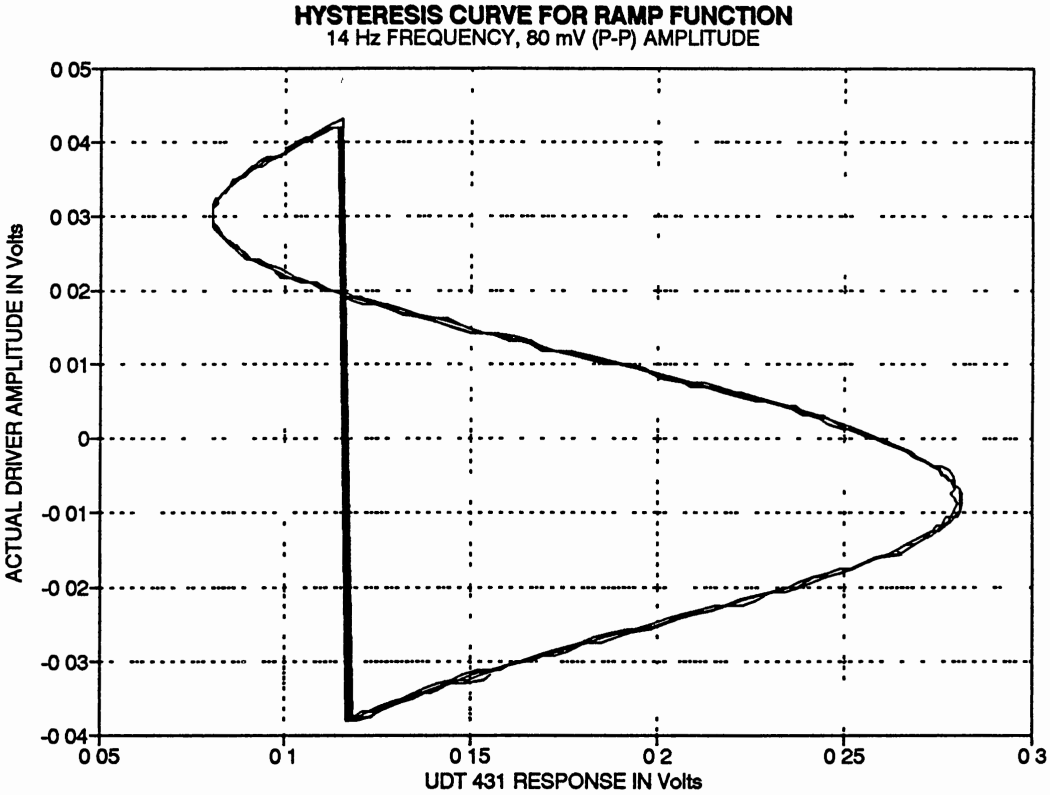

Figure 3 9 Hysteresis curve for Ramp driver function at 14 0 Hz driver frequency (resonance frequency) and 80 0 mV driver amplitude (P-P)

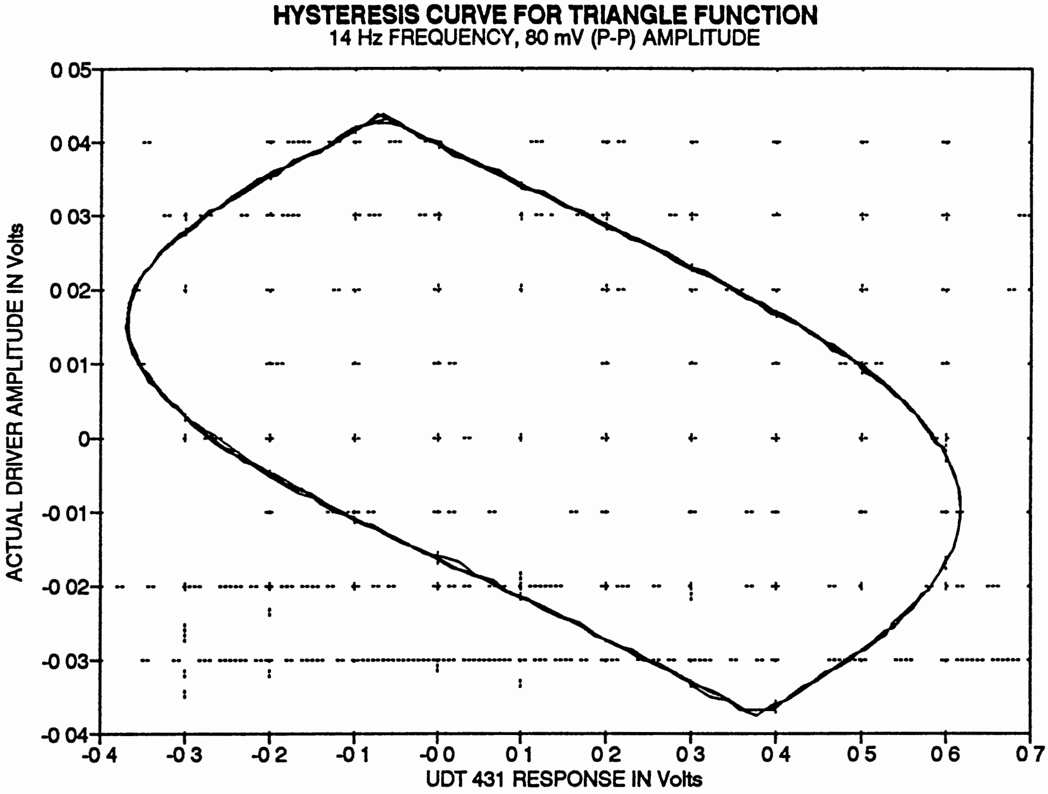

Figure 3 10 Hysteresis curve for Triangle driver function at 14 0 Hz driver frequency (resonance frequency) and 80 0 mV driver amplitude (P-P)

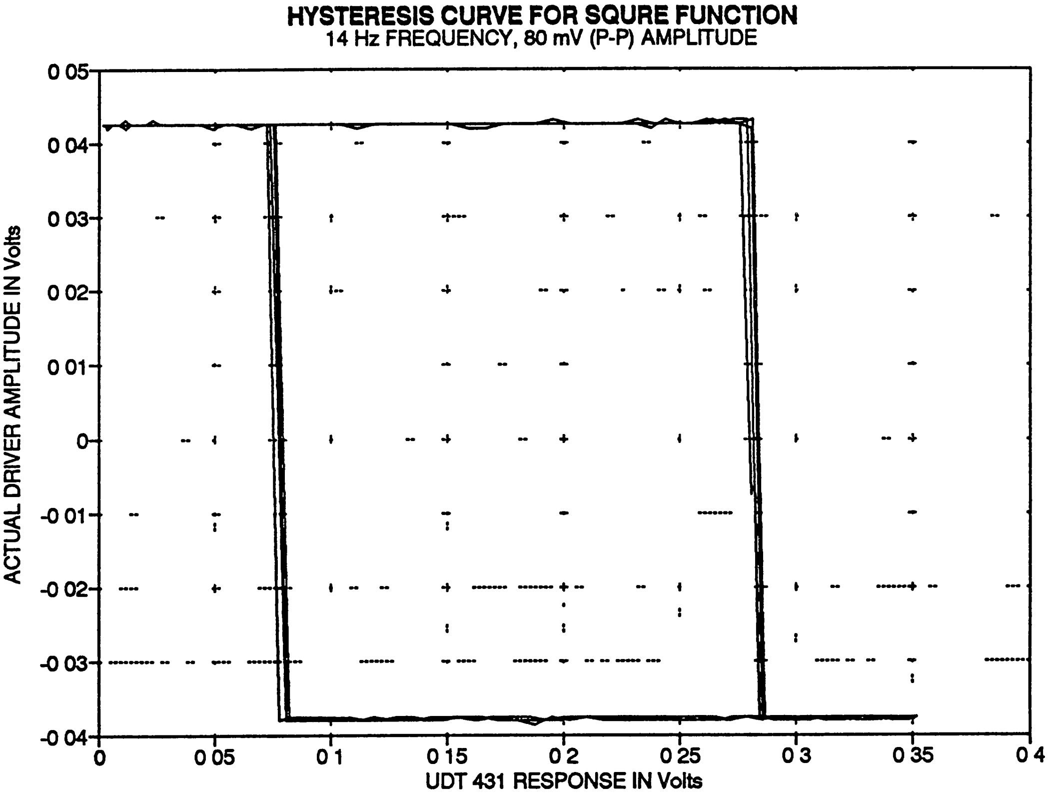

Figure 3 11 Hysteresis curve for Square driver function at 14 0 Hz driver frequency (resonance frequency) and 80 0 mV driver amplitude (P-P) function is clearly inappropriate for use in this case due to the large discontinuities in the response of the galvanometer. The deviation from the applied waveform is the lowest in the case of the triangle driver waveform and a significant portion of the response curve is linear. This indicated that as long as the galvanometer was operated within this linear range, the variation in the angle of mirror M_2 would also be very nearly linear with time. The significance of this observation was that a non-linear time dependence of the galvanometer response would affect the calibration of the wavelength axis of the final spectrum.

Determination of the Resonance Frequency of the GM-734 Galvanometer

The resonance frequency of the galvanometer as reported in the specifications provided by the manufacturer was 120 Hz (Table 3.1). The resonance frequency of the galvanometer as calculated theoretically was found to be 180 Hz. This apparent discrepancy, which can only be attributed to incorrect manufacturer specifications was resolved by experimental determination of the resonance frequency of the galvanometer. The experimentally determined value of the resonance frequency was found to be 174.9 Hz. A small sliver of glass from a microscope slide, weighing only about 0.1 g, was glued to the shaft of the galvanometer about half-way from the top. The galvanometer was rigidly fastened to the optical breadboard. The beam from the He-Ne laser was made incident on this sliver of glass at an angle of incidence of approximately 45° . The reflected beam from this sliver of glass was directed to the UDT LSC 5D detector head connected to the UDT 431 X-Y Position Indicator. The X-position output of the UDT 431 was connected to input channel 1 of the Data 6000 spectrum analyzer. The output signal of the HP 3325A function generator was amplified and then used to drive the GM-734 galvanometer and to trigger the Data 6000.

The driver amplitude was fixed at 400.0 mV (P-P) (sinusoidal driver function). The driver frequency was varied from 1.0 Hz to 200.0 Hz in increments of 0.5 Hz and the maximum and minimum amplitude values of the sinusoidal signal obtained from the UDT 431 were monitored. At the resonance frequency, the amplitude of oscillation of the galvanometer attained a maximum value, and this was reflected in the value of the maximum of the monitored signal. A resonance frequency of 175 Hz was obtained. The experiment was repeated with the driver frequency being incremented in units of 0.1 Hz in the range 160.0 Hz to 180.0 Hz, and this yielded a value of 174.9 Hz for the resonance frequency of the galvanometer. In addition to obtaining the true value of the resonance frequency of the galvanometer, it was also determined that in the range of frequencies from 1.0 Hz to 300.0 Hz, the galvanometer exhibited the presence of only one natural frequency. A plot of driver frequency vs measured amplitude (from the UDT 431) for the GM 734 galvanometer alone is shown in Fig. 3.12.

It was also necessary to determine the resonance frequency of the mirror-galvanometer combination as used in the interferometer. The theoretically calculated value of this resonance frequency was 17.0 Hz. This theoretically obtained value was experimentally verified by repeating the above procedure for

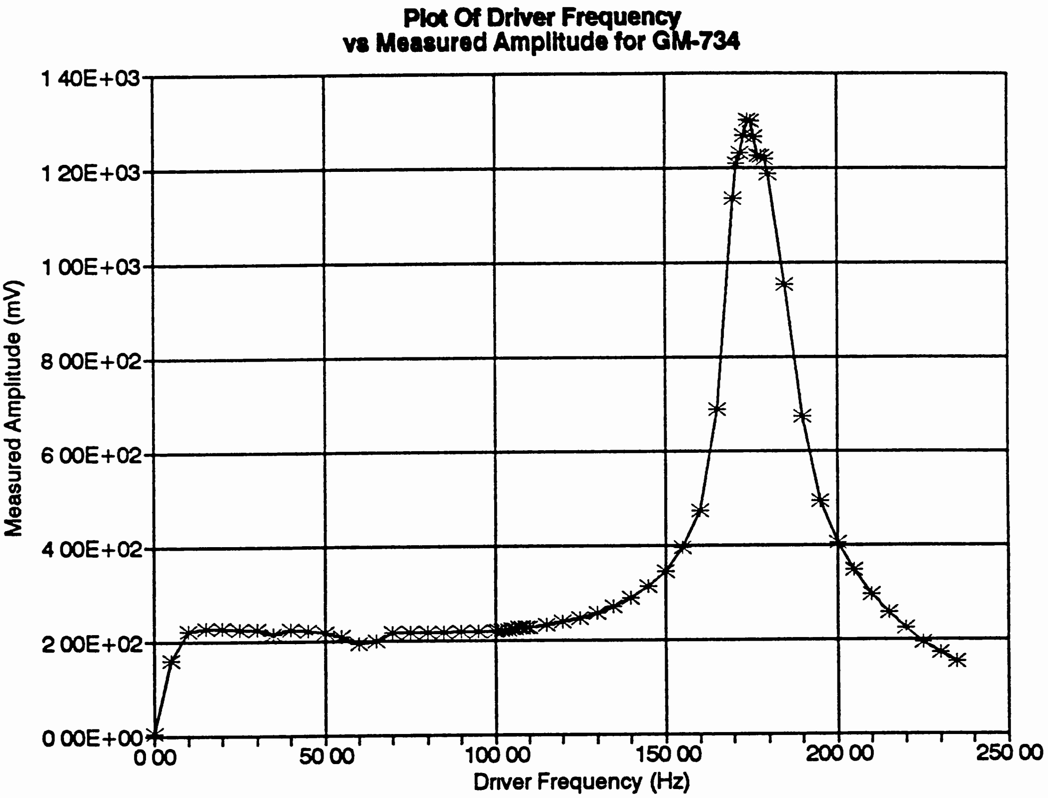

Figure 3 12 Plot of driver frequency vs measured amplitude for GM-734 Galvanometer (without mirror), showing a resonance frequency at 174 9 Hz the determination of the resonance frequency of the mirror-galvanometer combination (mirror M_2 in the interferometer). The experimentally determined value of the resonance frequency for the mirror-galvanometer combination was 14.4 Hz. A plot of the driver frequency vs measured amplitude (from the UDT 431) for the GM 734 galvanometer - mirror combination is shown in Fig. 3.13. In accordance with the theory of the dynamics of rigid bodies, the resonance frequency was seen to drop as the moment of inertia of the object attached to the galvanometer shaft was increased.

The response of the phase of oscillation of the galvanometer as a function of the frequency of the driver was measured. This was necessary to fully characterize the galvanometer and also provided yet another method for independently verifying the resonance frequency of the galvanometer. The output from the He-Ne laser was directed on to a plane mirror. The reflected beam was then made incident on the center of the mirror mounted on the GM-734 galvanometer (mirror M_2 in the interferometer). The beam reflected from this mirror was then directed on to the UDT LSC 5D detector head attached to the UDT 431 position detector. The x-position output from the UDT 431 was fed into input channel A of a Stanford Research Systems Model SR530 Lock-in Amplifier. The GM-734 was driven by the HP 3325A function generator. The amplified driver signal was also fed into the reference channel of the lock-in amplifier. The phase angle of the driver function was set to 0.° The driver amplitude was fixed at 600 mV (P-P). Using the sine driver function, the phase

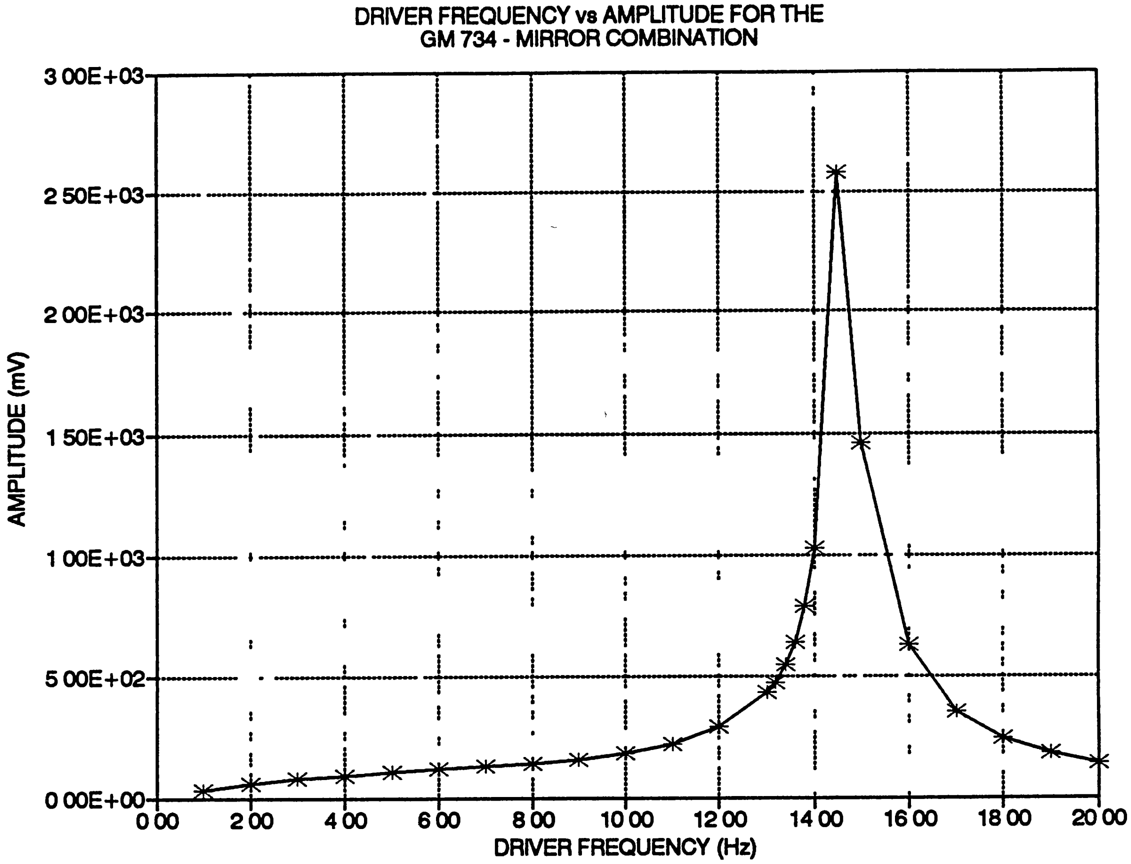

Figure 3.13 Compliance curve for the GM-734 Galvanometer showing the single resonance frequency

angle was measured as a function of the frequency. The frequency was varied from 1.0 Hz to 120 Hz. The measured phase angle was then plotted as a function of ratio of the driver frequency to the resonance frequency (Fig. 3.14). The phase angle as a function of the driver frequency, represents the time by which the applied force leads (or lags) the resulting vibration. The zero crossing of the phase angle in Fig. 3.15 indicates the resonance frequency of the galvanometer-mirror M_2.

Another method of determining the resonance frequency of a rigid body is by measuring its "compliance" and plotting this as a function of the driver frequency. Compliance is defined as the susceptibility of a structure to motion as a result of an external force, expressed quantitatively. Compliance curves are log - log plots of the compliance expressed in units of displacement/unit force vs driver frequency in Hz. Compliance can be expressed in terms of the following expression

$$C = \frac{|d|}{|F|}$$

where

C is the compliance

|F| is the magnitude of the applied force

|d| is the magnitude of the amplitude of the resulting displacement.

In general the compliance of a body depends on the frequency, position

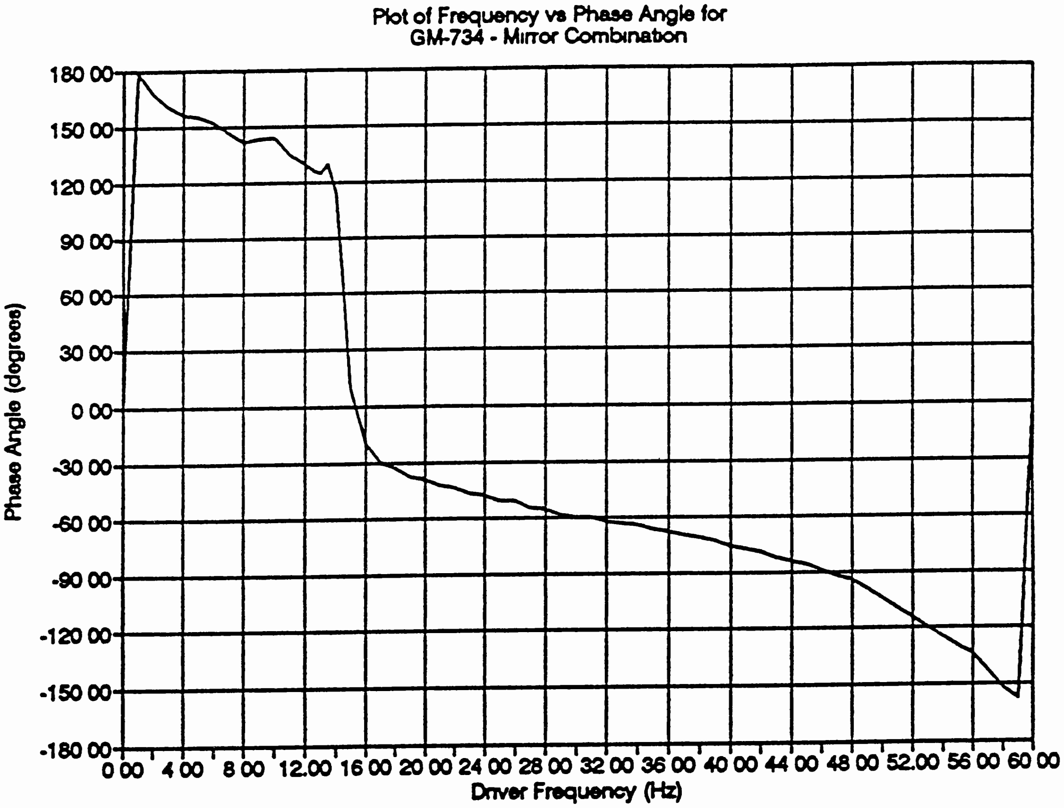

Figure 3 14 Plot of frequency vs phase angle response of GM-734 Galvanometer-Mirror (M_2) combination The graph shows the zero phase angle crossing at the value of the resonance frequency of the Galvanometer - mirror combination (approximately 15 Hz) and direction of the applied force. For an ideal rigid body the compliance is proportional to the inverse of the square of the driver frequency and is denoted by a straight line with a slope = -2 on a log - log plot described above. Application of this phenomenon to non-rigid bodies leads to the generation of a compliance curve which shows the body's resonance frequencies and associated damping characteristics. Fig. 3.15 shows the compliance curve for the GM-734 galvanometer. The compliance was calculated on the basis of the mass of the rotor shaft. This compliance curve shows the existence of only one resonance frequency, confirming the results obtained from the other experiments. Further, the value of the resonance frequency calculated from the compliance curve was in good agreement with the results obtained from the other experiments.

On the basis of the experimental evidence, 14.0 Hz was chosen as the operating frequency for this galvanometer. The static power consumption of the galvanometer at this driver frequency was calculated. The drive coil resistance of the galvanometer as provided in the specifications was 27.0 Ω. The amplitude of the driver function used to drive the galvanometer was 200.0 mV (P-P). The maximum value of the applied voltage was governed by the specifications of the galvanometer. Thus by Ohms law, the static current at full excursion at the applied voltage was given by

$$I = \frac{V}{R} = \frac{100.0 * 10^{-3}\ V}{27.0\ \Omega} = 3.70\ mA$$

where 100.0 mV is the voltage at full excursion in this case. Thus the static

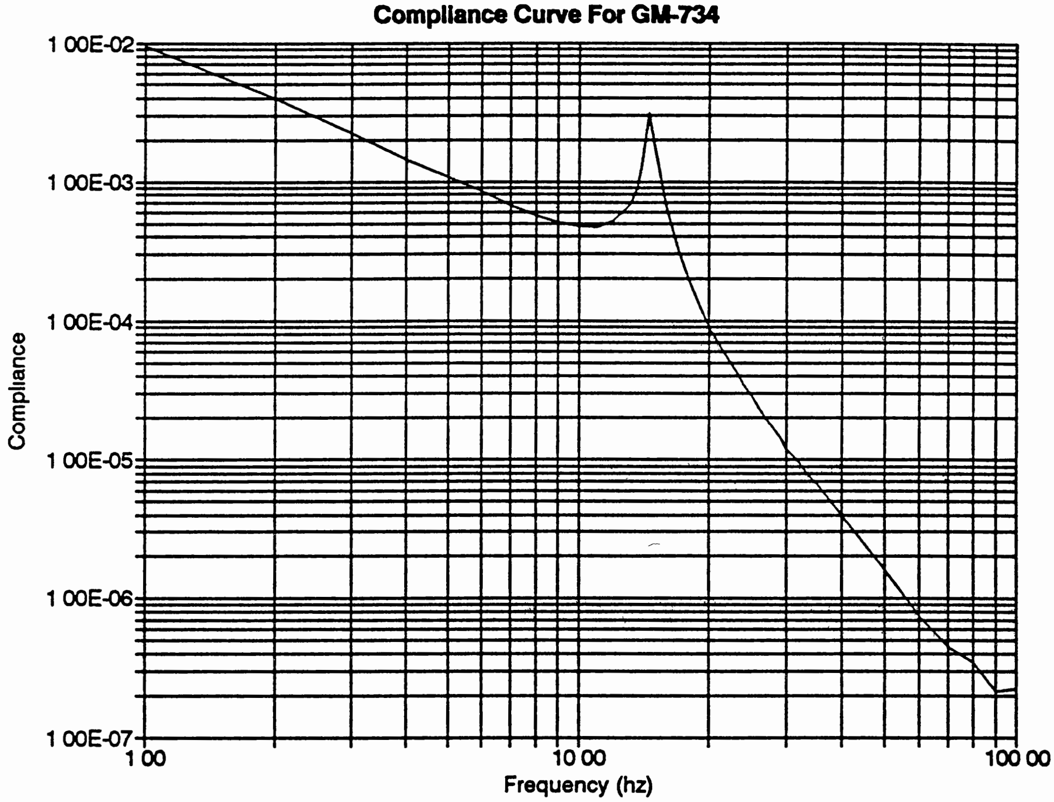

Figure 3 15 Compliance curve for the GM-734 galvanometer current at full excursion for this applied voltage is 3.70 mA. Now, calculating the static power we get

$$P = V\,I = I^2 R$$

$$= (3.70\mathrm{x}10^{-3})^2 A^2 \ \mathrm{x}\ 27.0\ \Omega = 0.369\ \mathrm{mW}$$

Thus the static power consumption at full at a driving amplitude of 200.0 mV (P-P) is only 0.369 mW. The AC power consumption of the galvanometer was also determined. In an AC circuit, the average power is given by

$$P_{av} = I_{rms} V_{rms}\ \mathrm{Cos}\phi$$

where I_{rms} and V_{rms} are the rms current and the rms voltage, and

$$I_{rms} = 0.707\ I_m\ ;\ V_{rms} = 0.707\ V_m$$

with I_m and V_m being the maximum values of the current and voltage respectively. Since Ohms' law holds for AC circuits as well, the power may be calculated as before and is given by

$$P_{av} = I^2_{av}\ R$$

$$= (0.707\ \mathrm{x}\ 3.70\mathrm{x}10^{-3})^2 A^2\ \mathrm{x}\ 27.0\ \Omega = 0.185\ \mathrm{mW}.$$

Determination of the Angle of Sweep of Mirror M_2

The He-Ne laser, the LSC 5D detector, and mirror M_2 were arranged in the form of an isosceles triangle, with mirror M_2 at the apex. The beam from the He-Ne laser was made incident on the center of mirror M_2. The reflected beam from the mirror was directed on to the LSC 5D detector head attached to the UDT 431 position detector. The X-axis output from the UDT 431 was fed into the input channel 1 of the Data 6000 Spectrum Analyzer. The reference input to the Data 6000 was the same signal used to drive the GM-734 galvanometer. The driver frequency was fixed at 14.0 Hz and the driver amplitude was varied from 10.0 mV to 200.0 mV. The amplitude of the signal observed on the Data 6000 was measured. The distances from the center of mirror M_2 to the LSC 5D detector and the He-Ne laser, and the distance from the LSC 5D detector to the He-Ne laser were also measured. The deflection from rest position of mirror M_2 was measured by measuring the deflection of the beam spot at the surface of the detector. The angle of deflection was calculated from this geometrical construction. The maximum deflection to either side of the nominal 45° position of mirror M_2 was found to be 0° 1'38.53".

The amplitude of the signal observed on the Data 6000 was plotted against the driver amplitude for a given driver frequency. The peak deflection of mirror M_2 with amplitude of the driver at 14 Hz was very nearly linear. This indicated that by varying the amplitude of the driver function, the maximum deflection angle, and thus the maximum path difference in the interferometer could be varied.

Acquisition of Spectral Data

The signal detected by the detector was processed and analyzed by a DATA 6000 Universal Waveform Analyzer. The waveform analyzer was capable of capturing the spectral data and performing a host of mathematical operations on the digitized data. The DATA 6000 also provided a convenient means of transferring the spectral data to an IBM AT compatible microcomputer for storage and presentation. This data transfer was accomplished by standard techniques and the integrity of the transferred data was extensively tested by means of software filters written in C. It was determined that in all cases, the integrity of the spectral data was retained and that there were no errors in the transfer of the data from the DATA 6000 to the microcomputer. Once stored on disk in the microcomputer, the data were readily available in the form of an ASCII data file and could thus be accessed by a variety of presentation and analysis software. Specifically, the Data 6000 was connected to a Cordata personal computer via the RS 232-C serial interface. (The Cordata was an IBM AT class microcomputer running Microsoft MS-DOS version 3.3 (48), and was equipped with a 20 megabyte hard disk drive). The spectral acquisition was carried out by first storing the spectral data in one of the display buffer memories of the Data 6000, and then downloading the intensity values into the hard disk drive of the Cordata with the aid of CROSSTALK version IV, communications software (MICROSTUF, Inc.). The data files were then transferred to a Gateway 2000 80386-33 MHz microcomputer (49). This IBM AT class computer was equipped with an 80 megabyte hard disk drive and an 80387 floating-point processor, operating under the MS-DOS version 5.0 (50) operating system (MICROSOFT Corp.). The data files were then transferred to BORLAND's QUATTRO PRO version 3.0 (51) spreadsheet software for final presentation.

Theoretical calculations were carried out with MATHCAD Mathematical software (MATHSOFT, Inc.) (52), running on the Gateway 2000 80386 computer under the WINDOWS 3.0 Operating Environment (MICROSOFT, Inc.) (53). The theoretical computation of the spectra was accomplished by a program written in C. This program written in BORLAND C++ (Borland Corporation), was compiled and executed on a Gateway 2000 80386/80387 microcomputer. The output of the program was stored as an ASCII data file and was also readily available for processing and presentation. All the theoretical and experimental spectra were plotted on a HP Laserjet Series II laser printer after being generated by the QUATTRO PRO (Borland Corporation) Spreadsheet and Graphics Software.

CHAPTER IV

RESULTS AND CONCLUSIONS

All the theoretical spectra were calculated on the basis of the theory presented in chapter II. It was shown that

$$S(\sigma) = \int_0^1 I(x) \; R(x) \; dx$$

where

$S(\sigma)$ is the spectrum of the source as detected at the detector, and

$$I(x) = \int_{\sigma_1}^{\sigma_2} S(\sigma) \; (1 + Cos(2\pi \Delta \sigma) \; d\sigma$$

is the spatial interferogram obtained with the interferometer, and

$$R(x) = \sum_{-\infty}^{\infty} c_n \; Cos \; (\frac{2\pi nx}{T})$$

is the function representing the Ronchi ruling, with

$$c_n = hsinc(nh) \; ; \; where \; sinc(x) = \frac{\sin(\pi x)}{\pi x}$$

The measured values for the spatial frequency of the Ronchi ruling (80 lines/cm) and the angle of deflection of the galvanometer mirror M_2 combination were used in calculating the theoretical spectra.

It was shown that the angle of deflection for any given wavelength of incident radiation required to produce interferometer fringes of the appropriate spatial frequency could be readily calculated from the equations (Eq. 2.53) derived earlier. This calculation was carried out for the He-Ne laser operating at 632.8 nm and the Ar^+ ion laser operating at a multiline output of 488.0 nm and 514.5 nm. At this value of the deflection angle for a particular wavelength, the spatial interferometer fringes would be transmitted through the grating and the resulting intensity would be recorded at the detector. The longest wavelength employed in this study was that of the He-Ne laser (632.8 nm). The angle of deflection required to study this wavelength was 1.1267×10^{-3} radians from the nominal position. The angle of deflection required to study wavelengths shorter than 632.8 nm, such as those from the Ar^+ ion laser was smaller than this value. For the 488.0 nm band from the Ar^+ ion laser, the required angle of deflection was 9.777×10^{-4} radians. On the basis of these calculations, the angle-to wavelength conversion factor was determined to be 1.9947×10^{-6} radians per nm.

In calculating the theoretical spectrum for the He-Ne-laser and the Ar^+ ion laser at full power, the range of the angle of deflection was 7.26×10^{-4} radians to 1.424×10^{-3} radians. Although the total deflection of the mirror M_2 in the interferometer has been restricted to 4.75×10^{-4} radians by design, larger values of the tilt angle could be obtained by providing an appropriate offset angle to mirror M_2. This could facilitate the potential use of the interferometer in a wide spectral range without compromising on the principle advantage of this design - very small movement of the mirror. Since the tilt angle for any given wavelength could be readily calculated from the equations derived earlier, the offset angle of mirror M_2 if any, could also be readily calculated. This offset angle could be set by measuring the spectrum of a standard source - for example a He-Ne laser for calibration of the offset angle in the visible spectral region.

Spectra of the He-Ne laser, the Ar^+ ion laser, and the combined spectrum of both these sources were obtained with the interferometric system developed here. In each case, the galvanometer (and hence, mirror M_2) was driven at a frequency of 14.0 Hz and an amplitude of 80.0 mV (P-P). The driver function used in each case was the triangular driver function. The total angular deflection obtained under these conditions was $\pm$ 4.75 x 10^{-4} radians. This corresponded to an angular deflection of 1.1875 x 10^{-5} radians/mV. Thus, for a given driver voltage at a specific driver frequency, a direct calibration of the deflection angle with respect to the driver voltage could be made.

Figure 4.1 shows the experimentally obtained spectrum of the Ar^+ ion laser at maximum output power. In this spectrum of the Ar^+ ion laser at full power, the 488.0 nm and the 514.5 nm bands are clearly visible and are well separated. The wavelength axis was calibrated on the basis of the deflection angles calculated earlier. It is seen that the theoretical predictions and the experimental observations are in good agreement. The experimentally observed position of the 514.5 nm band is slightly shifted from the value predicted theoretically. It is likely that this slight inaccuracy is due to a small non-linear dependence of the galvanometer response to the driver waveform. While all theoretical calculations were carried out with the assumption of strict linearity, even a small deviation from the linear portion of the sinusoidal response curve of the galvanometer would affect the accuracy of the experimentally observed spectral features.

The intensities of the 488.0 nm and 514.5 nm bands in this experimentally obtained spectrum were in the ratio of about 1 (514.5 nm) : 2.2 (488.0 nm). This was found to be consistent with the ratio of intensities measured with the optical power meter which was 1 (514.5 nm) : 2.53 (488.0 nm). Comparing the experimental spectrum in Fig. 4.1 and the theoretical spectrum in Fig. 4.2, it is seen that the experimentally observed intensity ratio of the source wavelengths is the same as that predicted by theory and is also consistent with physically measured values of intensity. The experimental spectrum shown in Fig. 4.1 has 256 data points. In the spectral range represented here (400.0 nm to 700.0 nm), there are 220 data points, with a separation of 1.366 nm per data point.

In the experimentally obtained spectrum (Fig. 4.1), for the Ar^+ ion laser the resolution at 488.0 nm and 514.5 nm were calculated by obtaining the FWHH at the 488.0 nm and 514.5 nm bands and then dividing the appropriate wavelength by the FWHH. This yielded a value of about 60 for the resolution of the spectrum obtained with the new interferometer at a wavelength of 488.0 nm. This

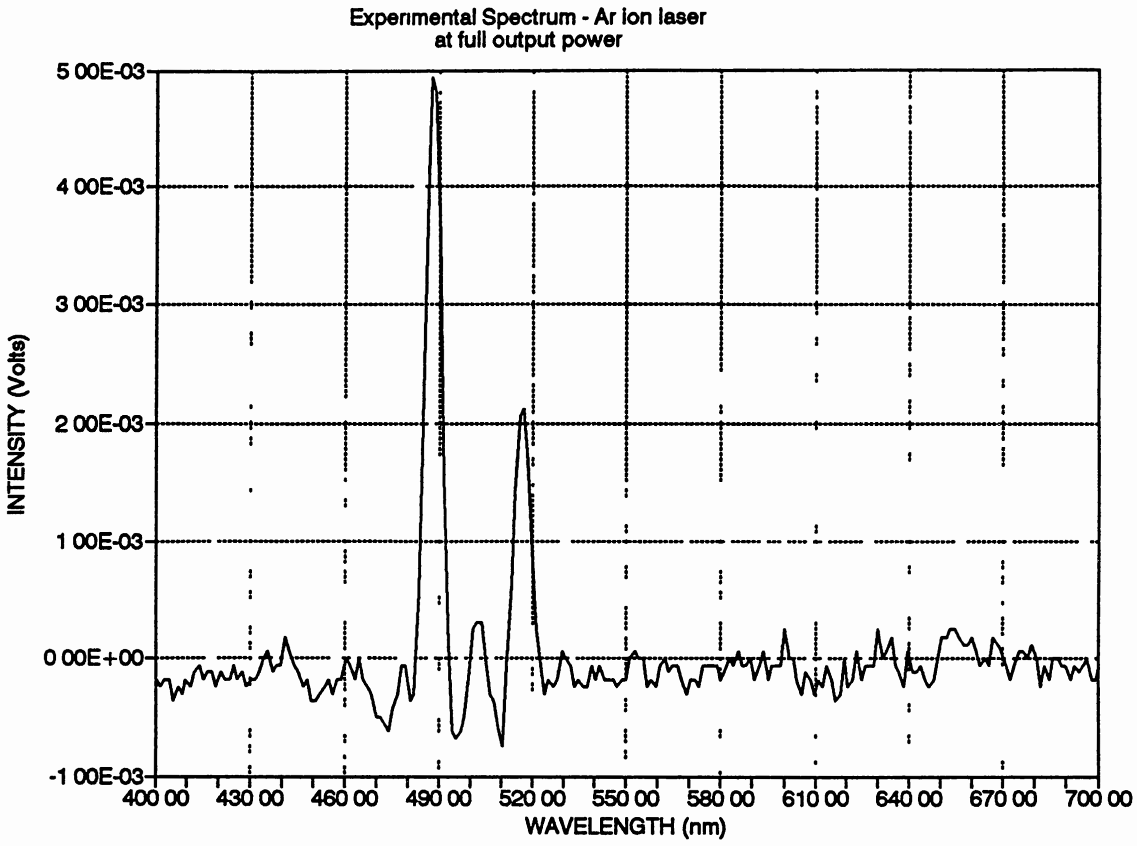

Figure 4 1 Experimental spectrum of Ar^+ at full power

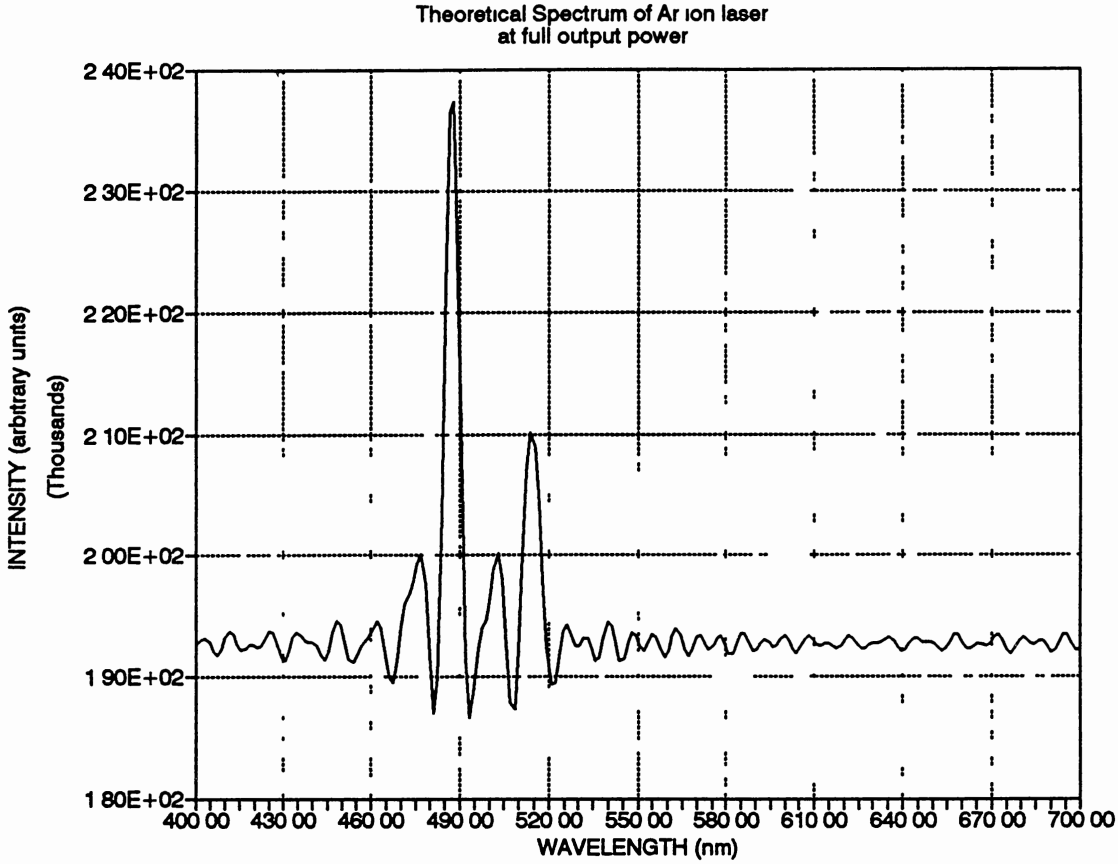

Figure 4 2 Theoretical spectrum of the Ar$^+$ laser at full output power can be compared with the theoretical spectrum for the Ar^+ ion laser at full output power shown in Fig. 4.2. In this theoretically obtained spectrum, the resolution at 488 nm is about 65. Fig. 4.3 shows the overlaid experimental and theoretical spectra for the Ar^+ ion laser, and Fig. 4.4 shows the experimental and theoretical spectra of the Ar^+ overlaid in the wavelength range of 450.0 nm to 525.0 nm.

Fig. 4.5 shows the experimentally obtained spectrum of the He-Ne laser. The resolution of this spectrum is about 50. Fig. 4.6 shows the theoretical spectrum of the He-Ne laser with a resolution of about 54. Fig. 4.7 shows the overlaid experimental and theoretical spectra, and Fig. 4.8 shows the overlaid experimental and theoretical spectra in the wavelength range of 600 nm to 650 nm.

Fig. 4.9 shows the experimental spectrum of the Ar^+ ion and the He-Ne lasers combined. This spectrum was obtained with both the sources turned on, and with the Ar^+ ion laser at full output power. Fig. 4.10 shows the overlaid experimental and theoretical spectra of the Ar^+ ion laser and the He-Ne laser.

It was observed that in all the experiments, the ratio of the intensities of the spectral bands was consistent with the ratio of the intensities as measured with a laser power meter. Further, the theoretically calculated spectra also predicted the same intensity ratios as those obtained experimentally.

The experimental spectra show some noise at the baseline. While some of this noise could be attributed to experimental causes, a significant percentage of

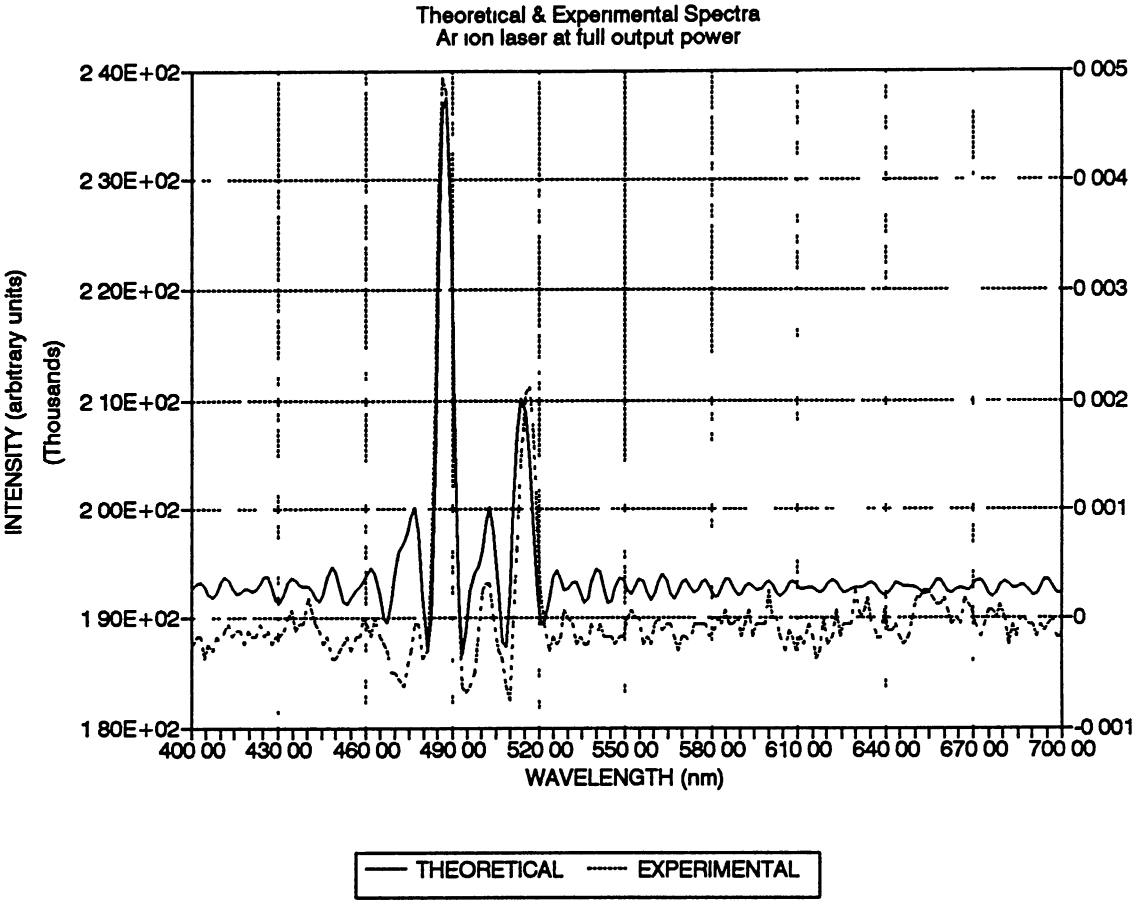

Figure 4 3 Theoretical and experimental spectra of the Ar^+ ion laser

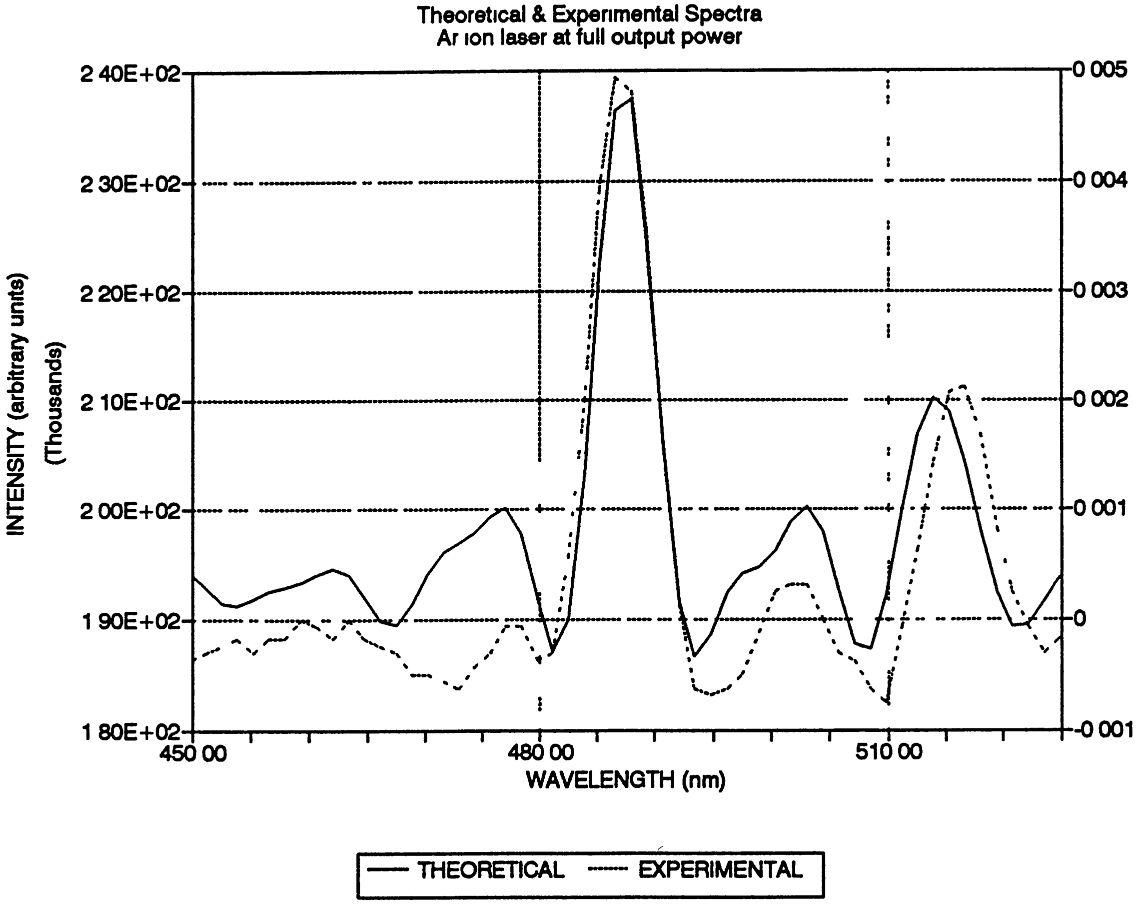

Figure 4 4 Theoretical and experimental spectra of the Ar$^+$ laser

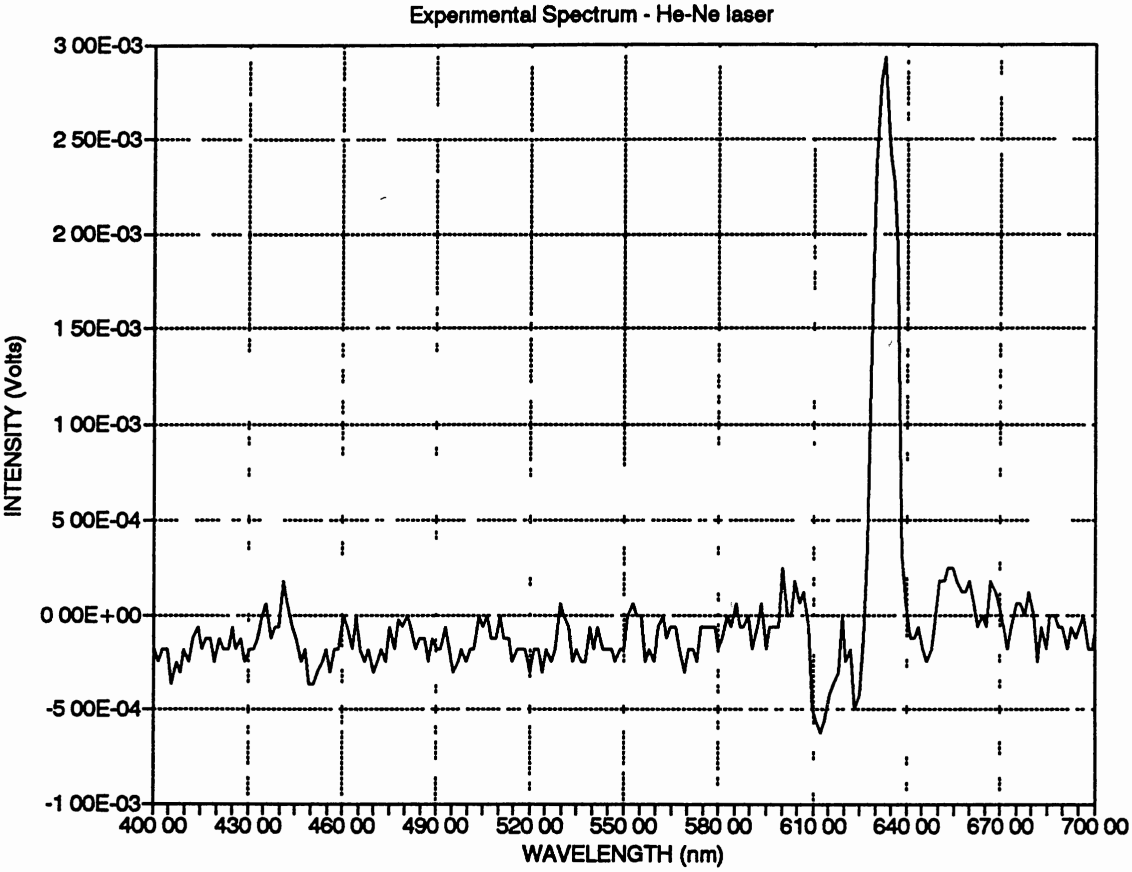

Figure 4.5 Expenmental spectrum of the He-Ne laser

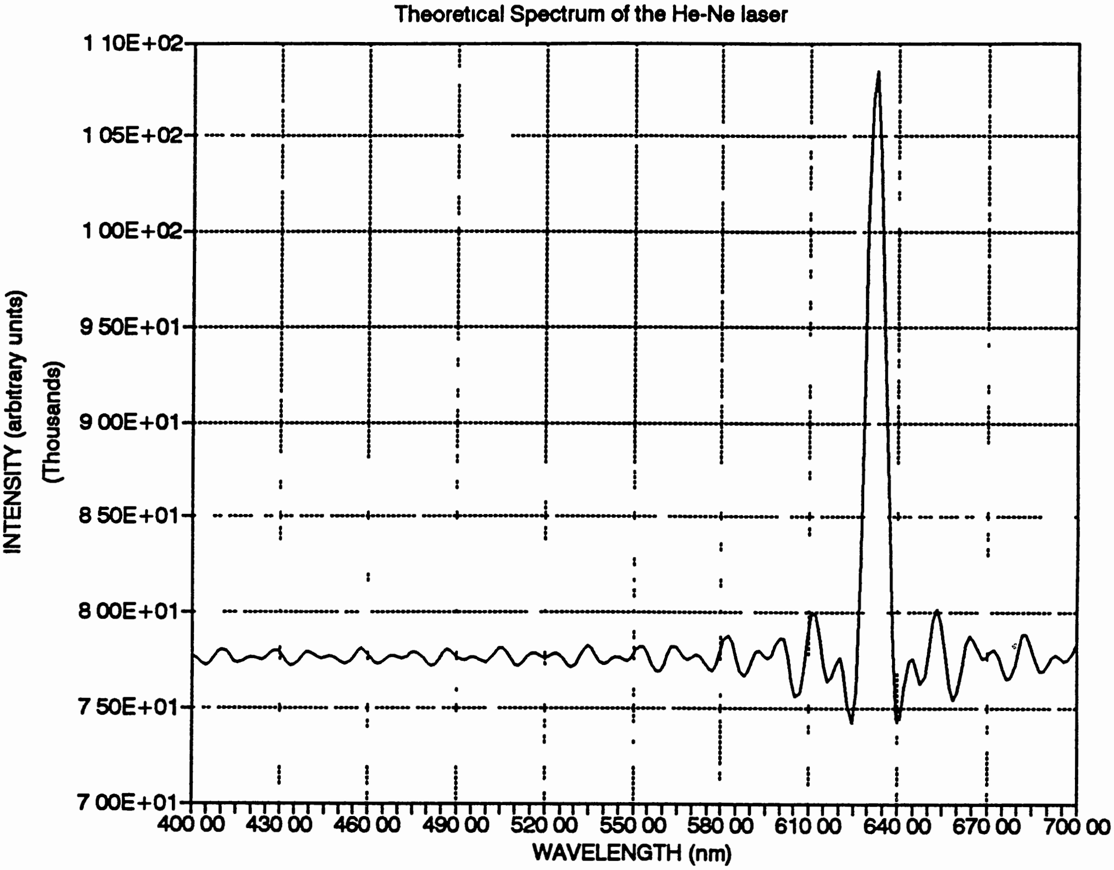

Figure 4 6 Theoretical spectrum of the He-Ne laser

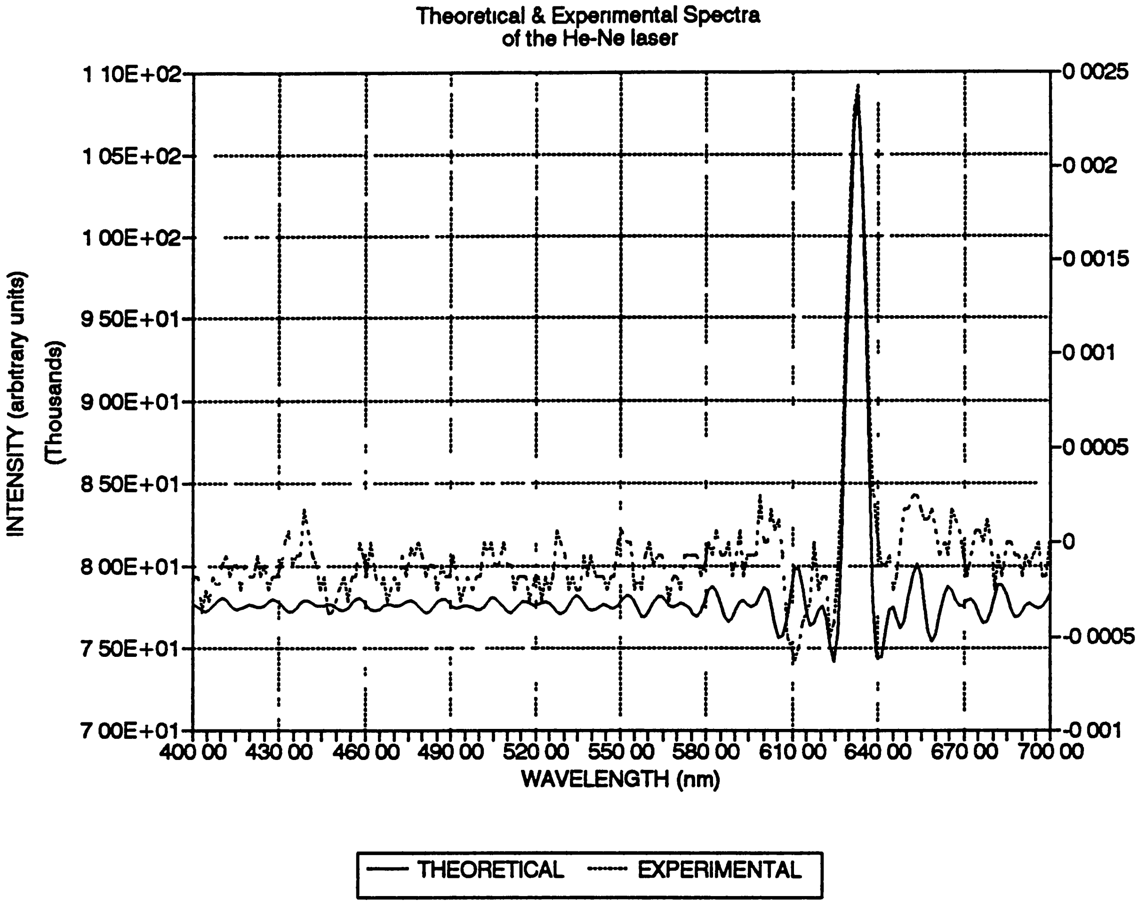

Figure 4 7 Theoretical and experimental spectra of the He-Ne laser

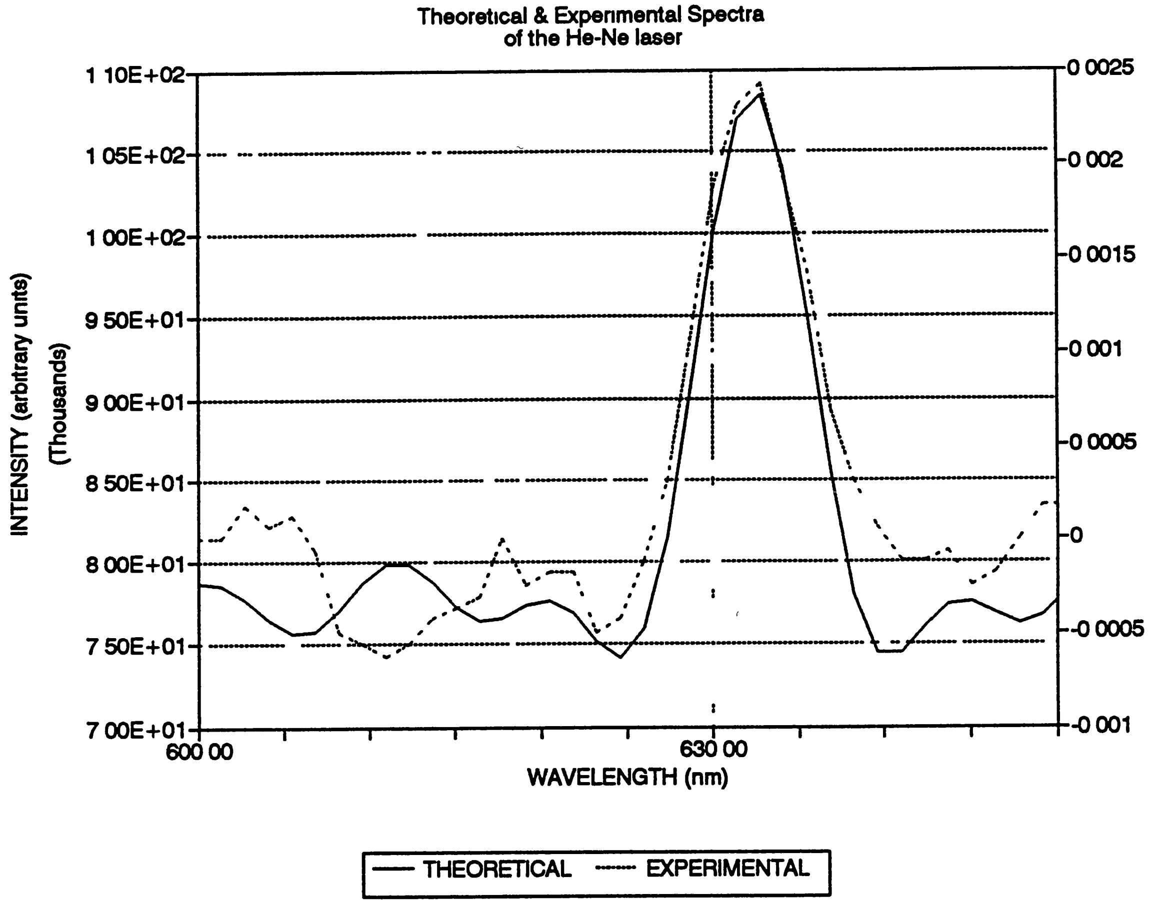

Figure 4.8 Theoretical and experimental spectra of the He-Ne laser

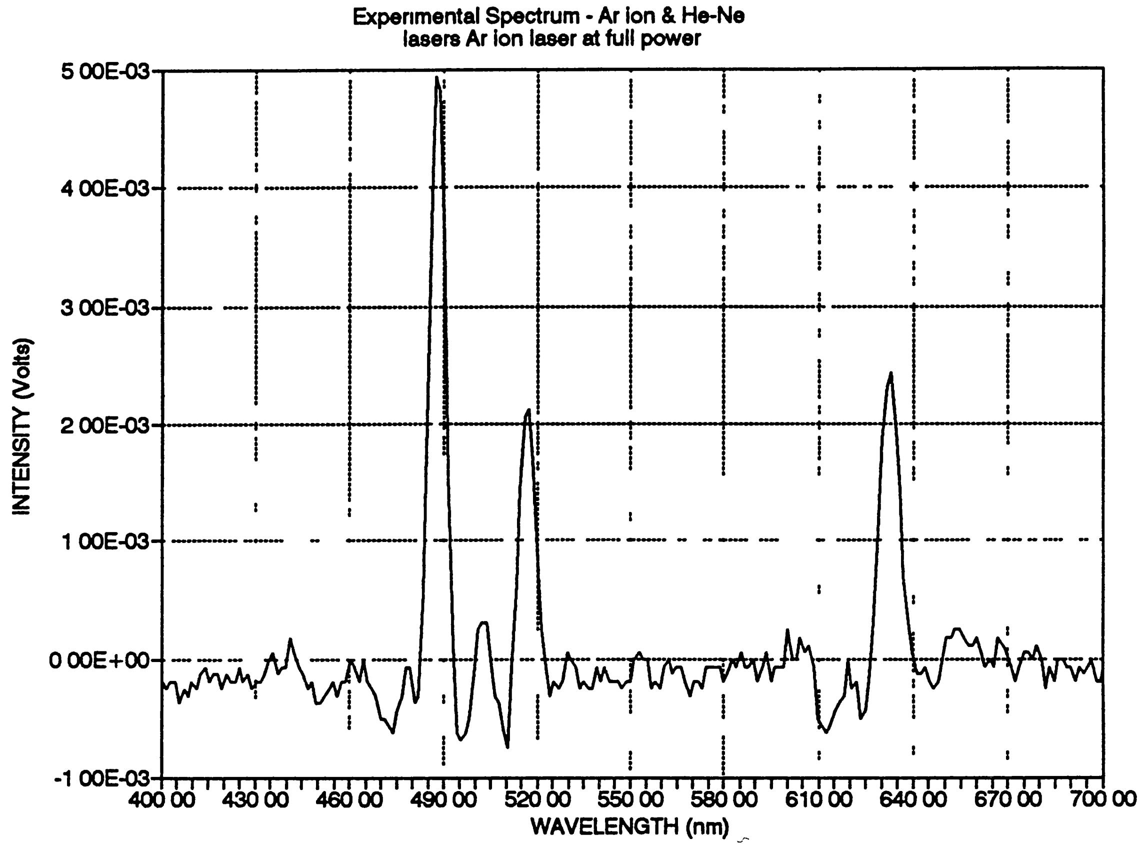

Figure 4 9 Experimental spectrum of the Ar^+ ion (full power) and He-Ne lasers

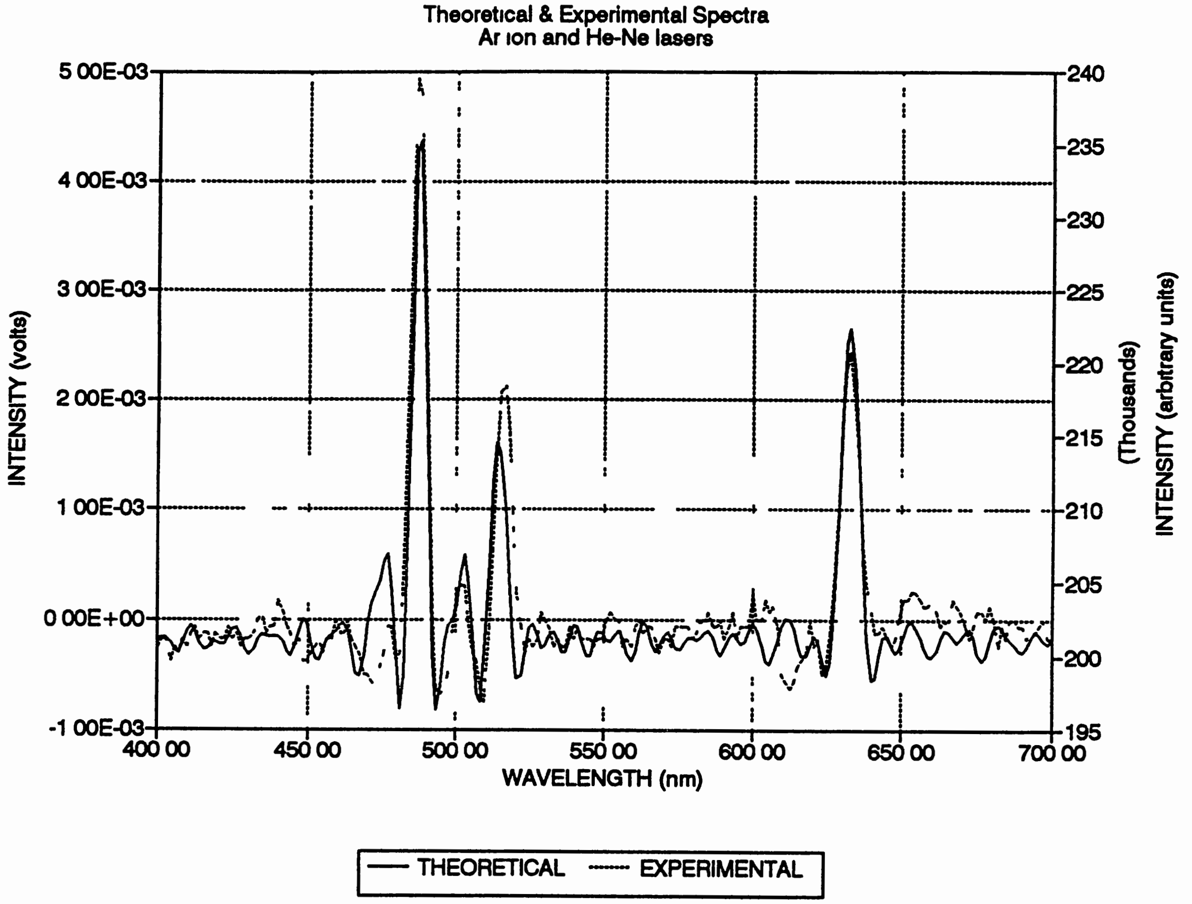

Figure 4 10 Theoretical and experimental spectra of the Ar^+ ion (full power) and He-Ne lasers the amplitude of the oscillations at the baseline is thought to be due to the presence of real spectral information. This can be understood by considering the functioning of the Ronchi ruling. The interference fringes formed at the Ronchi ruling are transmitted only if their spatial frequency matches that of the ruling. If the ruling were to be perfect, and the interferometer fringes were perfectly aligned in the vertical direction, then the only intensity that would be transmitted would be due to the incident radiation. However, even the highest quality Ronchi rulings have imperfections attributable to the manufacturing process. Added to this are the inherent effects of diffraction at the grating, which are unique to the grating used. Finally, contributions to the spectral intensities from higher diffracted order interferograms at the Ronchi ruling cannot be completely eliminated. All these factors contribute to the real and finite intensity measured at the baseline of the spectrum, thus making it appear noisy. This is not to suggest that the spectrum is totally noise free. Stray radiation, fan vibrations, dirty optical elements, and improper alignment all contribute to a noisy spectrum. In all the experiments reported here, detector noise is considered to be insignificant in comparison to the other noise sources.

Another major source of the finite intensity at the baseline in the experimentally obtained spectra and the theoretically obtained spectra is the very design of the interferometer. It was shown that the spectrum is obtained by the optical Fourier transformation of the spatial interferogram. This optical Fourier transformation is performed by the Ronchi ruling, which is square grating with some special characteristics. It was also shown that by Fourier theory, the spatial interferogram and the final spectrum are related by a Cosine Fourier transform. This implies that the use of Cosine grating in place of the Ronchi ruling would yield a spectrum which was exactly as predicted by theory. However, a Ronchi ruling was the closest approximation to a Cosine grating that was readily available and practical to use. This slight deviation from the ideal situation accounts for the noisy baseline in the theoretical and experimentally obtained spectra.

In light of the above facts, it is expected that signal averaging by coherent addition of multiple scans would not reduce the intensity at the baseline significantly. This is due to the fact that the intensity at the baseline is not truly "noise", but is in fact real spectral information. Signal averaging of 16, 32, 64, 128, and 256 scans did not show a significant decrease in the baseline intensity. This spectrum represents a single scan with no signal averaging. Since signal averaging did not improve the quality of the spectra obtained experimentally, it was not performed on any of the experimental spectra presented here.

Fig. 4.11 shows two single scan spectra of the He-Ne laser obtained under similar conditions but at different times. It is clear that the baseline intensity is not random noise.

Yet another feature of this interferometer that merits attention is the apparent phase reversal in the experimental spectra that is obtained under certain conditions. This phase reversal is directly linked to the spatial positioning of the Ronchi ruling, and is completely controllable. For instance, when the

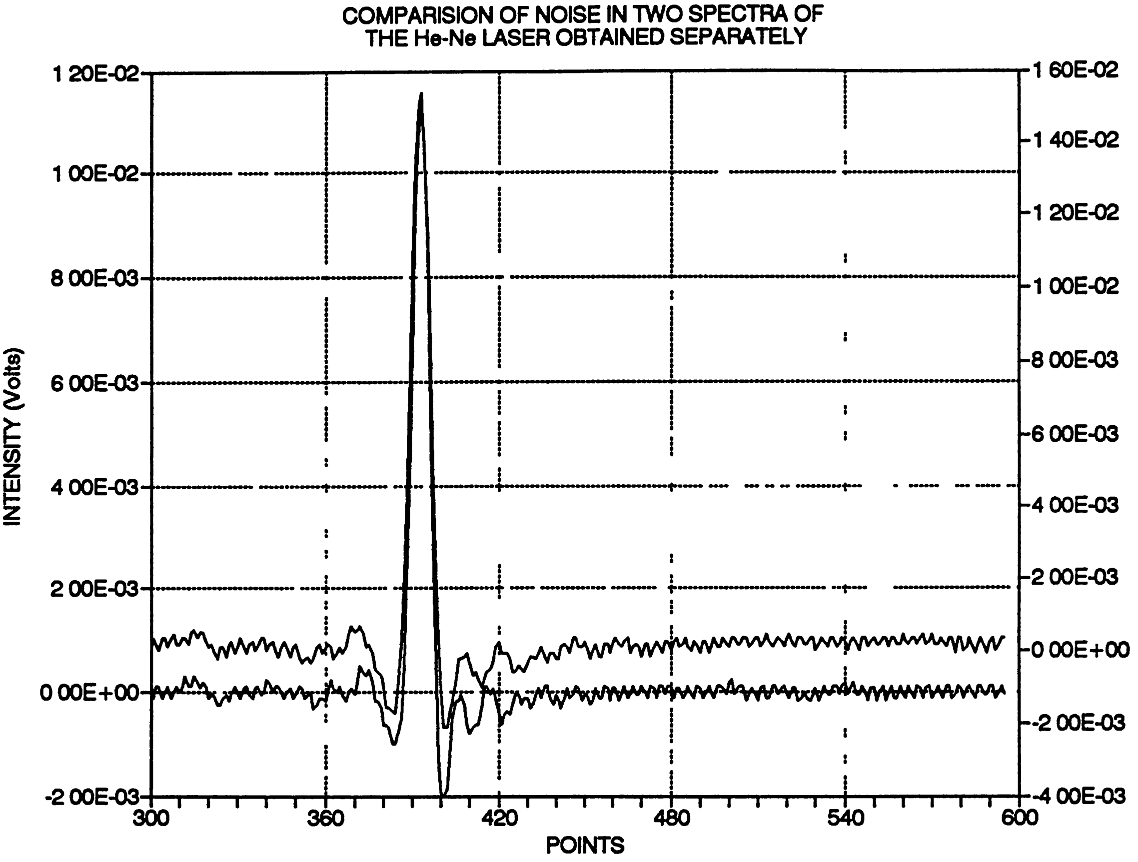

Figure 4.11 Experimental spectra of the He-Ne laser for noise comparison

Figure 4 11 Experimental spectra of the He-Ne laser for noise comparison

interferometer was adjusted to produce the spectrum of the He-Ne laser with the spectral band oriented in the spectrometrically correct orientation, a slight shift in the position of the Ronchi ruling would introduce a phase reversal of the spectral band. This slight shift in the spatial position of the Ronchi ruling was quantified, and corresponded to half a period of the Ronchi ruling. This phenomenon is of some importance in the overall experimental abilities of this interferometer, since it suggests that the interferometer may be suitable for absorption studies as well as emission studies.

Conclusions

The design, development, operating principles, and performance of a new type of spatial interferometer has been demonstrated. This interferometer has been shown to be appropriate for spectral acquisition in the 400-700 nm spectral range. Theoretical considerations indicate that this interferometer can be applied with a high degree of reliability and success for spectral acquisition in other spectral regions, most notably in the IR spectral region.

The interferometer, by its very design is extremely stable and is simple to operate and maintain. Changing the spectral window within a given spectral region is a simple matter and is readily carried out by introducing an appropriate offset in the tilt angle of mirror $\mathbf{M_2}$ in the interferometer. Switching to other spectral regions, such as the IR can also be readily performed by first modifying the optics of the interferometer, and then calculating the required tilt angle for mirror M_2, and the spacing of the Ronchi ruling. The changing of the optical components of the interferometer would also be a relatively simple matter due to the very nature of the design. It should be noted that with the wide availability of high quality, inexpensive single-element detectors for almost any region of the spectrum, and the availability of very high quality gratings with spatial frequencies from a few lines per cm to several thousand lines per cm, the interferometer developed here can be applied over a very wide spectral range. For example, an operational instrument with a resolution of 200 in the 800 cm^{-1} to 1200^{-1} (IR) spectral region would require a minimum angle of deflection of mirror M_2 of about 1.75×10^{-2} radians, with a grating with a spatial frequency of about 15 lines/cm. This study used a deflection angle of 4.75×10^{-4} radians and a Ronchi ruling with a spatial frequency of 80 lines/cm. The only other changes required would be the incorporation of suitable optical components for the IR spectral region (most importantly, the beamsplitter) and the selection of a suitable IR detector.

Although the Sagnac interferometer originated as a strictly non-moving parts interferometer, this study has shown that it can be adapted to have one so called 'pseudo non-moving part' - the scanning mirror driven by the galvanometer. It must be emphasized that this scanning element has very high stability when compared to moving mirrors driven by servo motors, or gas bearings or swinger arms, as is common in many of the more conventional FTIR instruments. This is in contrast to conventional Michelson-type interferometer based spectrometers, wherein the design aspects of the drive mechanism for the moving mirror constitute a major portion of all the design expenditure in terms of time, complexity, and money. As a result of the introduction of a simple and stable scanning mirror in the interferometer, significant simplifications could be made to the detection systems.

Most contemporary non-moving parts interferometers employ self-scanning or linear scanning photodiode array detectors (59,60). Such detectors are not suitable for use in low cost - low complexity systems. This is primarily due to the high cost of such detector systems, and the need for special operating conditions - such as cryogenic support etc., in the mid-IR for a high power HgCdTe array detector. In addition, array detectors used in non-moving parts interferometers impose a direct limitation on the resolution that can be achieved with such systems. In most systems with diode array detectors, the resolution is limited by the number of detector elements in the detector array, and the size of each detector element. In general, the higher the number of detector elements in the array that can be used in recording the spectrum, and the smaller the size of each detector element, the higher is the resolution that can be achieved. However, array detectors face a technological limit to the size of the individual detector elements that can be created in a given detector - and this is a direct limitation of the maximum possible resolution that may be achieved with such detectors. Currently, the size barrier seems to lie at or near the 10 micron range - commercial systems with detector spacings of less than this value are not yet available.

The significant advantage of the interferometer developed here over systems employing array detectors is that, with this interferometer a resolution of about 200 in the mid-IR can be obtained by employing a grating of spatial frequency 15 lines/cm, and using one of many single element detectors designed for the mid IR spectral region. The combined cost of a very high quality grating and single element detector for the mid-IR spectral region would be much lower than the cost of even the most modest array detector for the mid-IR region, and even the performance advantages of the array detectors such as increased effective etendue, do not provide a reasonable cost-to-performance ratio that can be justified for most of the applications discussed here.

By scanning one of the mirrors of the interferometer in an oscillatory motion, the need for a self-scanning array detector is eliminated, and a simple single element silicon photodiode detector can be employed. Specifically, the detector employed here costs $20.00, and the electronics needed to make it functional, costs an additional $10.00. However, these prices are applicable to photodiode detectors in the UV-Vis spectral region only. Detectors designed for operation in the mid-IR are significantly more expensive.

The resolution of this interferometer, while lower than that of a good Michelson-type instrument, is still sufficiently high for most routine work. While research grade instruments have achieved extraordinary resolving powers, and are the mainstay of fundamental research in the chemical, physical and biological sciences they also have very high costs - and therefore have limited applicability. Moreover, such high resolutions are usually not needed for all but the most difficult (i.e. spectroscopically) situations. Routine applications such as process monitoring and quality control, identification of samples with few chemical species, monitoring for atmospheric pollutants, and similar applications do not necessarily require resolution factors of much greater than 100.

It has been shown that the simple, inexpensive interferometer described here is easily capable of achieving this resolution. In addition, the wider applicability, reduced complexity of operation, and significantly reduced cost of such systems would offset any loss in resolution. It must be pointed out that from the outset, the design of the instrument described here was mandated by these factors, and not the desire to develop yet another high resolution spectrometer.

The single most important factor in determining the ultimate resolution of the interferometer is the spatial frequency of the Ronchi ruling - thus, the resolution of this interferometer can be improved significantly by simply upgrading to a Ronchi ruling with a greater number of lines/inch. In the instrument presented here, a resolution factor of 200 in the 400 nm to 700 nm spectral region may be achieved with a Ronchi ruling with about 700 lines/inch. Presently, Ronchi rulings with upto 5000 lines/inch are readily available at low cost. For example, a 2" x 2" Ronchi ruling with 5000 lines/inch is available from Edmund Scientific Corp. (Barrington, N.J.) at a cost of $397.00.

Perhaps the most significant feature of this interferometer is that it does not require any computational support to produce the final spectrum. In the configuration developed here, the regeneration of the final spectrum was carried out by optical methods (55-58), on the basis of Eq. 2.57. This was accomplished by the use of the Ronchi ruling, and the interferogram being a spatial variation of intensity rather than a signal in the time series. The impact of this one feature alone on the design of the interferometer is tremendous. It is inconceivable to think of a modern analytical instrument that does not incorporate sophisticated electronics and computer technology to carry out even the most basic of its functions. All this peripheral equipment, while not directly linked to the main function of the instrument, places the highest demands on the power consumption and the maintenance time required to keep the instrument functional. Thus, the elimination of almost all electronics and other computational hardware would significantly reduce the size, power consumption, maintenance, and down-time of any spectrometer incorporating this interferometer. Additionally, this feature would make it possible to obtain spectra in real time. Finally, the savings in cost realized by the incorporation of this feature would be very significant.

This interferometer has potential to meet all of the criteria set forth for an instrument of its type, namely, low cost, simplicity of operation and maintenance, low power consumption, reasonable spectral resolution and SNR characteristics, and the ability to withstand extremes in operating conditions.

Suggestions for Future Research

The resolution of the interferometer must be improved by incorporating Ronchi rulings with a higher spatial frequency than what has been used here. The interferometer, which has been shown to be functional in the visible region of the spectrum, must be extensively tested in the other spectral regions - particularly the IR. Suitable modifications in the design and optics must be devised to increase the efficiency and étendue of the interferometer. The étendue of this interferometer was calculated and was found to be about 0.326 mm^2 rad, assuming only a 50% loss of available radiation due to the beamsplitter. The actual étendue is likely to be significantly lower in light of defects in the optical components of the interferometer and the detector. The étendue of the interferometer must be calculated more rigorously. This will provide a basis for characterizing any improvements that may be made to the interferometer. Specifically, these improvements must include the incorporation of the highest quality optics (beamsplitters, mirrors, lenses) for the spectral region of choice. The mechanical components of the interferometer such as the mounting and connector rod for mirror M_2 must be made to adhere to closer design tolerances. Other mechanical components such as mirror and lens mounts must be specifically designed for this instrument so as to minimize any mechanical disturbances that may be present. Other detector systems such as the MCT detector and the InSb detector which can function both as a photoconductor and a photovoltiac detector in the mid-IR must be tested. The optimization of the present design must be carried out by subjecting the prototype instrument to extensive field testing. The results of such testing may yield valuable information on the performance of the individual components of the interferometer, provide a basis for improvements in its design and function, and serve to define the limitations of the instrument.

BIBLIOGRAPHY

1. Griffiths, Peter R., and de Haseth, James A., Fourier Transform Infrared Spectrometry, Elving, P. J., and Winefordner, J. D., (Ed.), CHEMICAL ANALYSIS, A series of monographs on analytical chemistry and its applications, a Wiley-Interscience Publication, v. 83. Chapters 1-7.

2. Rockley, M.G., Private Communications, (1991).

3. Ng, R.C.L, and Horlick, Gary, A Real Time Correlation-Based Data Processing System for Interferometric Signals, Applied Spectroscopy, 39:(5), 841-847, (1985).

4. Griffiths, Peter R., Transform Techniques in Chemistry, Plenum Press, New York, (1978).

5. Shibata, John H., and Johnson, Charles S. Jr., Theory of Holographic Relaxation Spectroscopy with Nonsinusoidal Gratings, Applied Spectroscopy, 39(5), 786-793, (1985).

6. Steel, W.H., Interferometry, The University Press, Cambridge, U.K.. (1967)

7. Stroke, George W., Coherent Optics and Holography,Second Edition, Academic Press, Inc, New York. (1969)

8. Hecht, Eugene and Zajac, Alfred, Optics, Addison-Wesley Publishing Company, Reading, Massachusetts. (1974)

9. Born, Max and Wolf, Emil, Principles of Optics, Pergamon Press, New York, (1964).

10. Malacara, Daniel, Analysis of the Interferometric Ronchi Test, Applied Optics, 29:(25), 3633-3637, (1990).

11. Hariharan, P., Optical Interferometry, Academic Press, Inc., Australia. (1985)

12. Bell, R.J., Introductory Fourier Transform Spectroscopy, Academic Press Inc., New York, (1972).

13. Chamberlain, John, The Principles of Interferometric Spectroscopy, John Wiley & Sons, New York, (1979).

14. Aryamanya-Mugisha, and Williams, Ronald R., A Fourier Transform Diode Array Spectrometer for the UV, Visible and Near IR, Applied Spectroscopy, 39:(4), 693-697, (1985).

15. Zachor, Alexander S., Drive Nonlinearities: Their Effects in Fourier Spectroscopy, Applied Optics, 16:(5), 1412-1424, (1977).

16. Kolczynski, J. D., Pomeroy, R. S., Jalkian, R. D., and Denton, M. B., Saptial and Spectral Imaging of Plasma Excitaion Sources, Applied Spectroscopy, 43:(5), 887-891, (1989).

17. Leith, Emmet N., Upatnieks, Juris and Haines, Kenneth A., Microscopy by Wavefront Reconstruction, Journal of the Optical Society of America, 55:(8), 981-986, (1965).

18. Stroke, G.W., and Funkhouser, A.T., Fourier Transform Spectroscopy using Holographic Imaging without Computing and with Stationary Interferometers, Physics Letters, 16:(3), 272-274, (1965).

19. Saccocio, Edward J., Applications of Lloyds Mirror to X-Ray Holography, Journal of the Optical Society of America, 57, 966, (1967).

20. Kamiya, K., Yoshihara, K. and Okada, K., Holographic Spectra Obtained with Lloyd's Mirror, Japan. J. Appl. Phys., 7, 1129, (1968)

21. Yoshihara, K., and Kitade, A., Holographic Spectra Using a Triangle Path Interferometer, Japan. J. Appl. Phys., 6, 116, (1967).

22. Dohi, T., and Suzuki, T., Attainment of High Resolution Holographic Fourier Transform Spectroscopy, Applied Optics, 10:(5), 1137 - 1140, (1971).

23. Yoshihara, K., Nakashima, K. and Higuchi, M., Holographic Spectroscopy using a Mach-Zehnder Interferometer, Japan. J. Appl. Phys , 15:(6), 1169-1170, (1976).

24. Okamoto, T., Kawata, S. and Minami, S., Fourier Transform Spectrometer with a Self-Scanning Photodiode Array, Applied Optics, 23:(2), 269-273, (1984).

25. Barnes, T.H., Photodiode Array Fourier Transform Spectrometer with Improved Dynamic Range, Applied Optics, 24:(22), 3702-3706, (1985).

26. Barnes, T H., Eiju, T., and Matsuda, K., Heterodyned Photodiode Array Fourier Transform Spectrometer, Applied Optics, 25:(12), 1864-1866, (1986).

27. Sweedler, J. V., and Denton, M. B., Spatially Encoded Fourier Transform Spectroscopy in the Ultraviolet to Near-Infrared, Applied Spectroscopy, 43:(8), 1378-1384, (1989).

28. Rockley, M.G., Private Communications, (1991).

29. Sweedler, J. V., Jalkian, R. D., and Denton, M. B. A Linear Charge-Coupled Device Detector System for Spectroscopy, Applied Spectroscopy, 43:(6), 953-962, (1989).

30. Zajac, A., Sadowski, H., and Licht, Seymour, Real Fringes in the Sagnac and Michelson Interferometers, Am.J.Phys., 29, 669-673, (1961).

31. Ronchi, Vasco, Forty Years of History of a Grating Interferometer, Applied Optics, 3:(4), 437-451, (1964).

32. O'Connell, Robert M., and Chen, Cheng-Hao, Ronchi Ruling Characterization of Axially Symmetric Laser Beams, Applied Optics, 29:(30), 4441-4446, (1990).

33. Mejias, P.M., and Herrero, Martinez R., Diffraction by One-Dimensional Ronchi Grids: On the Validity of the Talbot Effect, Journal of the Optical Society of America - A, 8:(2), 266-269, (1991).

34. Barnes, T.H., et. al, Grating Interferometer with Extremely High Stability Suitable for Measuring Small Refractive Index Changes, Applied Optics, 30:(7), 745-751, (1991).

35. Optics Guide 5, Melles Griot Inc., Irvine, California, (1991).

36. Optics and Filters Guide, ORIEL Corporation, Stratford, Connecticut, (1990).

37. Annual Reference Catalog for Optics, Science and Education, #11N1, Edmund Scientific Co., Barrington, New Jersey, (1991).

38. Newport Research Corporation, Research Catalog, Newport Research Corporation, Fountain Valley, California, (1990).

39. Operations Manual for General Scanning Model GM734 Open Loop Galvanometer, General Scanning Incorporated, Waltham, Massachussets, (1990).

40. Operations Manual for Model 2001 Argon Ion Laser, Uniphase Corporation, San Jose, California, (1990).

41. Operations Manual for ANDO Laser Power Meter, ANDO Corporation, USA, (1990).

42. Operations Manual for UDT 451 Photodetector, United Detector Technology, Hawthorne, California, (1988).

43. Operation Manual for Model 3325A Synthesizer - Function Generator, Copyright Hewlett-Packard Company, 1978, 1981, 1984; Marysville, WA 98270.

44. Operation Manual for DATA 6000 Universal Waveform Analyzer, Data Precision Division of Analogic Corporation, Danvers, MA 01923.

45. Operation Manual for CROSSTALK XVI, Data Communication Software System, Microstuf, Inc., Roswell, GA 30076.

46. Meriam, J.L., Dynamics, John Wiley & Sons, New York, (1966).

47. Torby, Bruce J., Advanced Dynamics for Engineers, Holt, Rinehart, and Winston, New York, (1984).

48. Operations Manual for MS-DOS, Version 3.3, Microsoft Corporation, Seattle, Washington, (1988).

49. Operations Manual for Gateway 2000, Model 80386 Microcomputer, Gateway 2000, Sioux City, South Dakota, (1991).

50. Operations Manual for MS-DOS, Version 5.0, Microsoft Corporation, Seattle, Washington, (1991).

51. Users Guide to Quattro Pro Version 3.0, Borland International Inc., Scotts Valley, California, (1991).

52. Users Guide to MathCAD, MathSoft Inc., Cambridge, Massachussets, (1991).

53. Users Guide to MS-Windows Operating System, Version 3.0, Microsoft Corporation, Seattle, Washington, (1991).

54. Users Guide to BORLAND C++, Version 2.0, Borland International Inc., Scotts Valley, California, (1991).

55. Mertz, L., Optical Fourier Synthesizer, J. Opt. Soc. Am., 46:(7), 548-551, (1956).

56. Mertz, L., Transformations in Optics, John Wiley & Sons, New York, (1965).

57. Lipson, H., Optical Transforms, Academic Press, New York, (1972).

58. Francon, M., Optical Image Formation and Processing, Academic Press, New York, (1979).

59. Winge, R.K., Fassel, V.A., and Eckels, D.E., Spectral Line-Diode Registry Effects with Photodiode Array Detectors, Applied Spectroscopy, 40:(4), 461-464, (1986).

60. Lepla, K.C., and Horlick, G., Data Processing Techniques for Improved Spectrochemical Measurements with Photodiode Array Spectrometers, Applied Spectroscopy, 44:(8), 1259-1269, (1990).

VITA

KAILASH SWARNA

Candidate for the Degree of

Doctor of Philosophy

Thesis: SELF-INVERSE TRANSFORMING PSEUDO NON-MOVING PARTS INTERFEROMETER: A THEORETICAL AND EXPERIMENTAL ANALYSIS

Major Field: Chemistry

Biographical:

Personal Data: Born in Madras, India, September 1, 1963, the son of S.V. Madhava Rao and Prema Rao.

Education: Graduated from DTEA High School, New Delhi, India, June 1980; received Bachelor of Science Degree, University of Madras, India, with a major in Chemistry, July 1983; received Master of Science Degree in Chemistry from Oklahoma State University, at Stillwater in July, 1988; completed requirements for the Doctor of Philosophy Degree at Oklahoma State University in December, 1991.

Professional Experience: Graduate Teaching Assistant, Oklahoma State University, 1985-1991; Graduate Research Assistant, Summer 1986, Summer 1987.